



**UNIVERSITÀ  
DI TRENTO**

Dipartimento di  
Fisica



# **NANOSCIENCE LABORATORY HIGHLIGHTS 2022**



*Image on the front cover: The packaged photonic chip under the objective of the spinning disk microscope*  
Photo by C.Zaccaria

## NANOSCIENCE LABORATORY

### MEMBERS (2022)

#### Faculty staff

Lorenzo Pavesi (full professor, head)  
 Marina Scarpa (full professor)  
 Zeno Gaburro (associate professor)  
 Paolo Bettotti (associate professor)  
 Stefano Azzini (associate professor)  
 Mattia Mancinelli (researcher)  
 Beatrice Vignoli (researcher)  
 Stefano Biasi (researcher)

#### Technical staff

Enrico Moser  
 Elvira D'Amato

#### Post-docs

Ilya Auslender  
 Alessio Baldazzi  
 Tiziano Facchinelli  
 Francesca Pischedda  
 Nicolò Leone  
 Clara Zaccaria  
 Bülent Aslan  
 Hum Nath Parajuli (left February 2022)

#### Administrative staff

Chiara Rindone (on maternity leave since April 2022)  
 Camilla Kandamulla Arachchige

#### Doctoral students

Davide Bazzanella (left june 2022)  
 Riccardo Franchi  
 Giovanni Donati  
 Matteo Sanna  
 Asiye Malkoç  
 Seyedeh Yasaman Heydari  
 Paolo Brunelli  
 Chiara Michelini  
 Emiliano Staffoli  
 Gianmarco Zanardi

#### Master students

Alessandro Zecchetto  
 Giorgio Letti  
 Alessandro Foradori  
 Diego Piciocchi  
 Stefano Gretter  
 Lorenzo Cerini

## SCIENTIFIC MISSION

### Introduction to the Nanoscience Laboratory

The Nanoscience Laboratory (NL) is one of the scientific groups of the Department of Physics, University of Trento. Its main areas of research are neuromorphic photonics, integrated quantum photonics, linear and nonlinear silicon photonics and nanobiotechnologies. The mission of NL is to generate new knowledge, to develop understanding and to spin-off applications from physical phenomena associated with photons and their interactions with matter, particularly when it is nanostructured. Specifically, NL aims at understanding the optical properties of lighthwave systems such as optical waveguides, microresonators and complex dielectric systems. NL covers the whole value chain from fundamental phenomena to device applications, where the photonic platform is compatible with the main driving silicon microelectronic technologies. However, silicon is not the only material studied. Other fields of interest concern the use of cellulose to tailor the properties of nanostructure atom-by-atom or the use of perovskites to investigate

their new properties.

NL research group consists of more than 20 people with different scientific backgrounds. Researchers from physics, physiology, bio-chemistry, materials science and electrical engineering are gathered to form a group of interdisciplinary nature. It is worth mentioning that NL collaborates closely with the Center of Materials and Microsystems, Fondazione Bruno Kessler (FBK). This collaboration spans over the last thirty years and covers various topics such as fabrication, testing and application of biomaterials and silicon based devices. Both participate in many common projects. The current one is project EPIQUS. A strategic collaboration is ongoing with the Trento units of CNR-INO, specifically dedicated to implement quantum optics in integrated silicon chip.

Moreover, with the support of FBK and CNR and every odd year, NL organizes a winter school on optoelectronics and photonics. The 12<sup>th</sup> edition will be "PQIP 2023 – Photonic Quantum Information Processing" in early 2023. Furthermore, the members of NL are often invited to participate in the organizing committees of international conferences or workshops.

The research activities of NL are mainly supported by the local government (PAT), by the European Commission, by the Italian Ministry of Education, University and Research (MIUR) and by companies. During the period covered by these Highlights, NL has been and is involved in the following projects: PRIN-MIUR PELM “Photonics Extreme Learning Machine: from neuromorphic computing to universal optical interpolant, strain gauge sensor and cancer morphodynamic monitor”; PRIN-MIUR PANACEA “A technology Platform for the sustainable recovery and advanced use of Nanostructured Cellulose from Agri-food residues”; ERC-2017-ADG-788793 BACKUP: “Unveiling the relationship between brain connectivity and function by integrated photonics”; H2020-FETOPEN-01-2018-2019-2020 EPIQUS Electronic-photonic integrated quantum simulator platform; Q@TN project “Quantum Science and Technology in Trento”; India-Trento Program for Advanced Research - ITPAR: “A cheap, light, compact source for QKD based on intraparticle entanglement in an integrated photonic circuit”; ASI - LESSO: “Laser etero-integrato a stato solido per trappole ottiche”; NANOFARM (Legge Provinciale 13 dicembre, 1999 n. 6).

### Silicon Nanophotonics

Silicon photonics is the technology where photonic devices are produced by standard microelectronic processes using the same paradigm of electronics: integration of a large number of devices to yield a high circuit complexity, which allows for high performances and low costs. Here, the truth is to develop photonic devices that can be easily integrated to improve the single device performance and to allow high volume production.

We will mostly concentrate on two alternative approaches where photonics is used to compute. On one side we will develop new scheme to implement artificial intelligent in a photonic silicon chip by using brain-inspired or neuromorphic computing schemes. On the other side, we will use silicon photonics to provide a suitable platform for quantum computing and quantum simulations. In both approaches, one fundamental device is the silicon microresonator where whispering gallery modes induce nonlinearities, which can be exploited to generate new quantum states of light or to realize recurrent neural network. In addition, we use micro-disks or micro-rings to study new physics (chirality, frequency comb generation, entangled photon generation). The microresonators are coupled directly with narrow mode SOI (Silicon-on-Insulator) waveguides. Also, multimode waveguides are used for nonlinear frequency conversion or generation.

To develop silicon photonics, one further add-on is making silicon to do something that it is not able to do in its standard (bulk) form. Low dimensional silicon, where small silicon nanocrystals or nanoclusters (Si-nc) are developed, is one way to compel silicon to act as an active optical mate-

rial. Alternatively, we use the built-in or p-i-n induced electric fields to tune the non-linear optical properties of silicon waveguides for the development of new MIR sources (parametric generation via second order effects or frequency comb generation). Nonlinear optics is finally used to generate pairs of entangled photons, which in turn feed quantum interferometers or integrated quantum photonic circuits.

Lastly, hybrid chips are developed to interface living neurons with photonic waveguides in the search for artificial intelligence. Here, the signal transduction is achieved by using photo-sensitive proteins.

### Advanced nanomaterials for energy, environment and life

In this research activity, we learn from nature how to use molecules or biological nanostructures to build materials with specific features. The focus is on understanding the properties of colloids of biological origin, the dynamics at the bio-interfaces, the strength and stability of natural structures. The final goal is to transfer the acquired knowledge on innovation by developing sustainable and smart materials and processes.

### Experimental facilities

The NL facilities allow for detailed experimental studies in nanoscience, photonics and biotechnologies. Since the effective collaboration with FBK most material processing and device productions are performed within their premises. For photonics, we have facilities to cover the light spectrum from the THz to UV ranges with whatever time resolution is needed. Laser sources comprehend: Ti-sapphire fs-ps laser (1 W average over 1000-700 nm, 2 ps or 70 fs pulses, 82 MHz repetition rate) interfaced with a second harmonic generator and pulse picker; TOPAS pumped with an amplified Ti:Sa laser which covers the 1-2.6  $\mu\text{m}$  range with 35 fs, 10 kHz, 3 mJ; 2W tunable CW Cr:ZnSe/S fiber-bulk hybrid laser to cover the 2-3  $\mu\text{m}$  range; four tunable CW lasers (850-870 nm, 1200 - 1700 nm and 1500 - 1600nm) fiber pig-tailed; high power fiber-laser at 1550 nm (1-100 MHz, 50 ps); 4W EDFA and 2W semiconductors amplifiers, a supercontinuum light source (410-2400 nm, 1W), several pig-tailed diode lasers, ASE source at 1550 nm and a broad band SLD at 800 nm; three high-power true-CW DPSS single-line laser operating at 532, 473 and 355 nm. Detectors comprehend: visible and infrared photomultipliers and CCDs, a visible streak camera with ps resolution, 4K cooled bolometers which cover THz region, avalanche photodiodes for vis and IR ranges plus many single photon detectors in the visible and IR. Two home-made MIR single photon-counters. To perform spectral analysis several set-ups are available: FTIR and dispersive spectrophotometers, a micro-Raman setup, a micro-FTIR and a UV-vis-IR spectrophotometer (shared with other laboratories), UV-Vis and fluorescence spectrophotometer dedicated to biochemical experiments. Eight set-ups are dedicated to the

characterization of waveguides equipped with nanopositioning systems and polarization controllers, each specified on a given function: visible, visible broad range, quantum, passive infrared, high speed infrared, non-linear infrared, non-linear MIR and on wafer. A set-up is dedicated to high speed measurements, with 80 Gbps capability where a 60 GHz arbitrary waveform generator, electro-optical modulators, coherent detectors and a four channels, 20 GHz oscilloscope. Other devices are: - a solar simulator for cells up to 5 inches in size; - two nanoprobe stations (AFM and SNOM) - two semiconductor probe stations (4 and 8 inches) and different electrical characterization systems (I-V, Z- $\Omega$ , EL-I, etc.). Four VIS to NIR optical spectrum analyzers are available. A probe station is interfaced by a fibres bundle with a spectrometer equipped with nitrogen cooled visible and IR CCDs. An electrochemical laboratory with various chemical hoods, galvanostats and volt-ameters is available for sample processing. For optical, electrical and molecular dynamics simulations, the laboratory uses free and commercial software and has a work-station with 4 GPU. Two laboratories are also available, one dedicated to chemical synthesis and the other to the preparation of biological samples. Two other laboratories with biological hoods, incubators and confocal microscopes are dedicated to biological experiments. In one, a confocal microscope with an insert for electrophysiology (MEA) and optogenetics measurement equipped with a "spinning disk" system for fast acquisitions and a super-resolution system.

### 2022 Publications

- N. Leone, S. Azzini, S. Mazzucchi, V. Moretti and L. Pavesi "Certified quantum random-number generator based on single-photon entanglement", *Phys. Rev. Applied* 17, 034011 (2022)
- G. Donati, A. Argyris, C. Mirasso, M. Mancinelli, L. Pavesi, "Noise effects on time delay reservoir computing using silicon microring resonators", *Proc. SPIE 12004, Integrated Optics: Devices, Materials, and Technologies XXVI, 120040U* (5 March 2022)
- M. Sanna, D. Rizzotti, S. Signorini, L. Pavesi, "An integrated entangled photons source for mid-infrared ghost spectroscopy", *Proc. SPIE 12009, Quantum Sensing and Nano Electronics and Photonics XVIII, 120090L* (5 March 2022)
- R. Franchi, S. Biasi, F. Mione, L. Pavesi, "On the response of the Taiji microresonator against small perturbation of the counter propagating mode", *Proc. SPIE 12004, Integrated Optics: Devices, Materials, and Technologies XXVI, 1200406* (5 March 2022)
- C. Zaccaria, M. Mancinelli, B. Vignoli, I. Auslender, P. Bettotti, et al., "Light induced memory in in-vitro neuronal cultures ", *Proc. SPIE 11947, Optogenetics and Optical Manipulation 2022, 1194703* (7 March 2022)
- M. Mancinelli, D. Bazzanella, P. Bettotti, L. Pavesi, "A photonic complex perceptron for ultrafast data processing", *Scientific Reports*, 12:4216 (2022)
- S. Biasi, R. Franchi, F. Mione, L. Pavesi, "Interferometric method to estimate the eigenvalues of a non-Hermitian two-level optical system", *Photonics Research*, Vol. 10, No. 4, April 2022
- M. Borghi, L. Pavesi, "Mitigating indistinguishability issues in photon pair sources by delayed-pump intermodal four wave mixing", *Optics Express*, Vol. 30, No. 8, 11 April 2022
- S. Hassan, D. Chack and L. Pavesi, "High extinction ratio thermo-optic based reconfigurable optical logic gates for programmable PICs", *AIP Advances* 12, 055304 (2022)
- D. Bazzanella, M. Mancinelli M. Borghi P. Bettotti and L. Pavesi, "PRECISE Photonic Hybrid Electromagnetic Solver-PRECISE Photonic Hybrid Electromagnetic Solver", *IEEE PHOTONICS JOURNAL*, Vol. 14, no. 3, June 2022
- B. Vignoli and M. Canossa, "Perirhinal Cortex LTP Does Not Require Astrocyte BDNF-TrkB Signaling", *Cells*, Vol. 11, 1501 (2022)
- D. Bazzanella, S. Biasi, M. Mancinelli and L. Pavesi, "A Microring as a Reservoir Computing Node: Memory/Nonlinear Tasks and Effect of Input Non-ideality", *JOURNAL OF LIGHTWAVE TECHNOLOGY* (2022)
- S. Biasi, F. Franchi and L. Pavesi, "Interferometric cavity ringdown technique for ultrahigh Q-factor microresonators", *OPTICS LETTER* Vol.47 n. 16 (2022)
- Piccoli, M. Sanna, M. Borghi, L. Pavesi and M. Ghulinyan, "Silicon oxynitride platform for linear and nonlinear photonics at NIR wavelength", *OPTICAL MATERIALS EXPRESS* Vol.12 Issue 9 pp. 3551-3562 (2022)

- S. Biasi, R. Franchi, D. Bazzanella and L. Pavesi "On the effect of the thermal cross-talk in a photonic feed-forward neural network based on silicon microresonators" *Frontiers in Physics, Sec. Optics and Photonics* (2022)
- Bettotti, P. and Scarpa, M. (2022). Nanocellulose and its interface: On the road to the design of emerging materials. *Advanced Materials Interfaces*, 9(4) doi:10.1002/admi.202101593
- Checchetto, R., Scarpa, M., De Angelis, M. G. and Minelli, M. (2022). Mixed gas diffusion and permeation of ternary and quaternary CO<sub>2</sub>/CO/N<sub>2</sub>/O<sub>2</sub> gas mixtures in matrimid®, polyetherimide and poly(lactic acid) membranes for CO<sub>2</sub>/CO separation. *Journal of Membrane Science*, 659 doi:10.1016/j.memsci.2022.120768

#### 2022 PhD Thesis

Nicolò Leone, "A quantum entropy source based on Single Photon Entanglement" (26 April 2022)

Clara Zaccaria, "Light induced engrams in in-vitro neuronal cultures" (28 April 2022)

Davide Bazzanella, Microring Based Neuromorphic Photonics (23 May 2022)

#### Project web sites

<http://nanolab.physics.unitn.it/>

<https://r1.unitn.it/back-up/>

<https://r1.unitn.it/back-up/erc-poc-alpi-project/>

<https://epiqus.fbk.eu/>

<https://grange.eu/>

<https://sites.google.com/unitn.it/panacea/home>

<https://r1.unitn.it/pelm/>

<https://www.quantumtrento.eu/>

### 1. Cellulose-based nanomaterials (Marina Scarpa, Paolo Bettotti, Elvira D'Amato, Tiziano Facchinelli)

Cellulose is the most abundant biopolymer in the world (cellulosic residues in EU accounts for several tens of Mtonnes/year) and it is turning out to be one of the most promising renewable, sustainable and biocompatible material as the nanoscale engineering of such ancient material continues to reveal unexpected properties. Cellulose has a multiscale architecture made by highly intertwined fibrils, each formed by elementary building blocks, the cellulose nanocrystals (CNC), bind together by amorphous flexible regions.

CNCs are highly stable and easy to produce from cellulosic waste, this fact eases the possibility to investigate different properties and to exploit CNC for different applications.

In the last years we deepened our knowledge on the synthesis and properties of both CNCs and CNC-based hydrogels and their possible use. This work has been summarized into a review article [Bettotti P., Scarpa M., "Nanocellulose and Its Interface: On the Road to the Design of Emerging Materials", (2022) *Advanced Materials Interfaces*, 9 (4), art. no. 2101593].

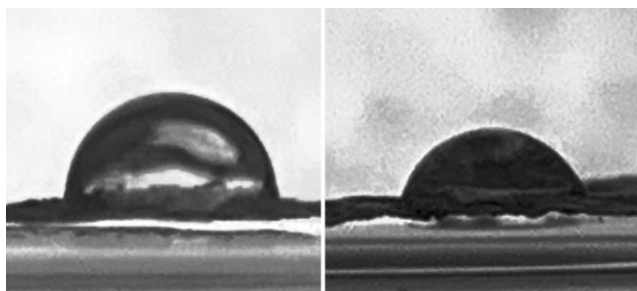


**Figure 1:** Contact angle of a droplet of water deposited over a gas selective CNC film. A side of this film was modified to increase the resistance to water vapor present in the permeant gas.

Last year we start new research activities on CNCs that were mainly finalized in writing project proposal and establishing new collaborations with research groups. The most important research plans foreseen are resumed here:

- CNC shows a strong piezoresponse and bring relevant amount of electrostatic charge. Thus it is a candidate material to develop energy harvester (EH) devices. EH are smart devices that by spilling tiny amount of energy from ubiquitous, intermittent and low power energy sources are able to convert this random movement into useful work. Currently three project proposals are under revision and we start collaboration with other groups on this topic.

- gas permeability of CNC films might be extremely low [Roilo D., Maestri C.A., Scarpa M., Bettotti P., Egger W., Koschine T., Brusa R.S., Checchetto R., "Cellulose Nanofibrils Films: Molecular Diffusion through Elongated Sub-Nano Cavities", (2017) *Journal of Physical Chemistry C*, 121 (28), pp. 15437 - 15447, DOI: [10.1021/acs.jpcc.7b02895](https://doi.org/10.1021/acs.jpcc.7b02895)]. By proper tuning of the chemistry of the film and of its structure, hybrid materials might find interesting use in the

field of selective gas separation, particularly for carbon dioxide sequestration. We start to collaborate with Italian groups with strong expertise on this field.

- CNC as artificial extracellular matrix (ECM). In this case CNC hydrogels will be used as substrate for cell cultures. "Synthetic" ECM has several advantages compared to "natural" counterparts, to cite few of the most important are the ease with which they are produced and the control over their composition. CNCs have high cell compatibility (Meschini, S, Pellegrini, E, Maestri, CA, et al. In vitro toxicity assessment of hydrogel patches obtained by cation-induced cross-linking of rod-like cellulose nanocrystals. *J Biomed Mater Res.* 2020 108B: 687– 697). Moreover the ionotropic gelation mechanism permit to tune easily the mechanical properties of the gel and, thus, its interaction with cells.

### 2. Random walk on a graph as a statistical model of memory engram formation (Gianmarco Zanardi, Luca Tubiana, Paolo Bettotti)

Biological studies of memory do and always have put significant emphasis on the existence of a memory trace: the engram. As of this day, modelling the dynamics leading to the formation of engrams is an open problem, as multiple possible models of long-term potentiation (LTP) of synapses have been investigated. On the biological side, there are cells other than neurons that might have a role in the formation of memory engrams: astrocytes. In the Nanoscience Lab, we are experimentally aware of a very peculiar neuron-astrocyte interaction that can be responsible for LTP. This interaction is stochastic and happens at the level of so-called "astrocytic microdomains"; we are trying to incorporate it in a model of biological memory.

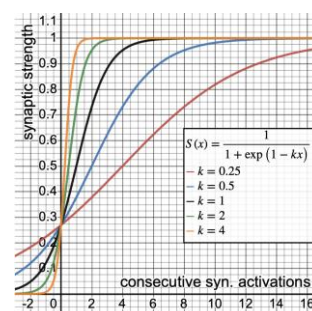


**Figure 2:** Synaptic strength  $S$  vs consecutive synaptic activations  $x$ . Logistic function-shaped synaptic strength according to the equation in the figure with different values for parameter  $k$  and fixed  $R = 1$ ,  $x_0 = 1$ . The larger the value of  $k$ , the steeper the curve for small values of  $x$  and therefore the faster it reaches the threshold value  $R = 1$

Over the last year, we have developed and continuously refined a statistical model for engram formation based on random walk on a graph. The model is agnostic to the biological reality of the brain; however, it is robust enough for proper statistical considerations, yet simple enough to capture a qualitative picture of engram formation. We

have built our random walk dynamics such that, when the walker traverses an edge of the graph, it induces a temporary increase of its weight for future steps of the walk. These dynamics mimic the synaptic strengthening that happens inside the brain when strong stimulations form a memory engram. In this picture, then, an engram would appear as the repeated use of the same path of edges over time. Moreover, we can cluster multiple edges together and introduce a stochastic contribution that resembles the work of astrocytic domains mentioned above.

Our specific implementation is a discrete-time random walk on a cyclic feed-forward neural network<sup>1</sup> (NN). We regularise the walk-induced weight growth by applying a logistic function  $S(x)$  to a linearly increasing hidden variable  $x$  that is related to the number of consecutive uses of an edge (i.e., consecutive synaptic activations). The specific function is  $S(x) = \frac{R}{1 + \exp(x_0 - kx)}$  where  $x$  is the hidden variable and  $R$ ,  $k$  and  $x_0$  are parameters that control the shape of the function, hence the dynamics of our system. The model also features an exponential decay term that fights memory. Edge clusters, representing astrocytic domains, are placed onto the NN in a “renormalisation group” fashion: each one wraps four neighbouring edges. We implemented these clusters as having a “meta-plastic” effect on the dynamics: they stochastically (0.5 probability in each timestep) increase the rate at which weights grow, affecting the parameter  $k$  as depicted in Figure 2. In our model, only few selected clusters are set to interact with the NN; all other clusters are silent.

We tasked our system to store a pattern of nodes by allowing only those clusters involved in the pattern to be active. We considered different combinations of values for the parameters of our system (e.g., characteristic time  $\tau$  for the decay term, threshold value  $R$  of weights) and performed multiple simulations for each combination. We analysed the results in terms of a pattern distance over time w.r.t. the tasked pattern, comparing the individual nodes in the patterns as well as the edge clusters involved. Figure 3 shows the mean distances over 50 iterations of the system in a “positive” (i.e., favourable) condition for memory (largest  $\tau$ , large  $R$ , large  $\Delta x$ , largest initial  $k$ ). The resulting mean distances reflect this aspect: they improve both at the node- as well as at the cluster-level after an initial time window because clusters are all silent when simulation starts and settle to a constant value well before the half-time of the simulations. Node-level-wise, the distance remains substantial, settling between 0.6 and 0.7, but the steadiness suggests the system has indeed stored something that is however not the exact pattern it was tasked to.

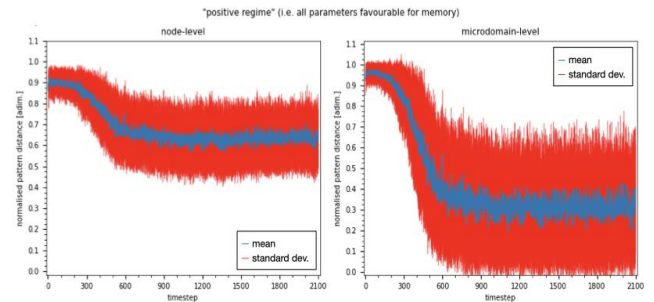


**Figure 3:** Pattern distances over time w.r.t. the tasked pattern in a “positive” regime of parameters. Distances are computed at two “resolution levels”: comparing individual nodes (left) and comparing astrocytic microdomains (i.e., edge clusters) (right). Both distances visibly improve after an initial time window of about  $100 \div 200$  timesteps, settling to a constant value around timestep  $600 \div 800$ .

The cluster distance, settling below 0.5, suggests that more than half of the microdomains of the stored pattern match those of the tasked one: the tasked and the stored patterns are not very distant, i.e., dissimilar, when seen at the coarser resolution level of edge clusters.

### 3. Light induced activation of an in vitro neuronal engram (Clara Zaccaria, Asiye Malkoç, Beatrice Vignoli)

The term memory refers to the storage of knowledge that can be recalled by the brain. It is commonly assumed that information is stored in the brain as physical lasting alterations of a group of neurons, simultaneously excited, known as an engram, whose permanent modifications include the reinforcement of synaptic connections (long-term potentiation and depression, LTP and LTD) and/or the increase in the number of spines among a specific set of neurons during memory trace encoding (Poo M.M et al., 2016; Josselyn et al. 2020). One of the goals of the BACKUP project is to use patterned light illumination to generate a memory engram in a small *in vitro* neuronal network. The idea is to create an artificial engram utilizing optogenetic technologies in which light illumination will imitate the activation of a group of interconnected neurons expressing channelrhodopsins. In this way, patterned light will function as an artificial learning event for the generation of memory engrams.

Cortical neurons were prepared from mouse embryos, and infected with pAAV-Syn-ChR2(H134R)- YFP at days in vitro (DIV) 3-4. To be able to generate an artificial engram by using patterned light-illumination we must be able to specifically illuminate and consequently activate simultaneously specific neurons of the network. With this aim, neurons at DIV 11-13 were stimulated with light spots created by a digital light processing (DLP) device. The setup is shown in

<sup>1</sup> The network can be pictured as laying on a genus-1 torus, where each layer of nodes belongs to one radial cross-section plane of said torus.

Figure 4A. The light spots were drawn on single neuronal body and were designed to be larger than the average neuronal soma diameter (10 μm), yet small enough to excite only one neuron (Figure 4B). The spots created by the 10x objective have an FWHM of  $47 \pm 8 \mu\text{m}$ , and a contrast of  $(14 \pm 6) \times 10^3$ ; the spots created by the 20x immersion objective have an FWHM of  $27 \pm 7 \mu\text{m}$  and a contrast of  $(17 \pm 8) \times 10^3$ . Contrast is defined here as  $((\text{Max}-\text{Min})/\text{Min}) \times 100$ . The minimum distance to consider the two spots independent was calculated projecting two spots at different distances (Figure 4D) and normalizing the maximum intensity of the spots on the background (C), and on the intensity level between them ( $\Gamma$ ). The data shown in Figure 4D, representing the ratio  $C/\Gamma$ , go to saturation at about 60 μm with 10x objective and about 100 μm with 20x objective.

The optical power that reaches the sample depends on the DLP's and objective's relative alignment, as well as the focal length of the objective. Additionally, the power delivered from the LEDs can be varied by adjusting its driving current. The average power coming at the sample was measured under the microscope objectives, with a power meter. The average intensity on the sample plane is then obtained through a normalization on the illuminated area. The distribution of light on the sample plane, however, is uneven, which means that once an operating power is selected from the LEDs of the DLP, neurons in different positions in the field of view (FOV) will receive different light intensities, affecting equal optogenetic excitation of the illuminated cells. We modified the light distribution loading 8-bit depth images to compensate for the non-homogeneity of light excitation. To do so, the wide-field light intensity distribution on the sample plane is acquired and loaded in the software (Figure 4E). Once the required pattern is generated, it is normalized across intensity, which means that the 8-bit image delivered to the DLP will be less intense when the power delivery is higher and more intense where the reverse happens. As can be seen in Figure 4E, in this way the light distribution is flattened. Due to the DLP's non-linear conversion of the 8-bit pixel values in intensity, the intensity at the border lowers by at most 50% of the maximum, which is still enough to excite the neurons if a proper intensity starting value is chosen.

To ensure that the intensity is sufficient to excite neurons in the whole FOV, we set a LED current average intensity of about 13 mW/mm<sup>2</sup>. Using this setup parameters, we performed calcium imaging experiments using X-Rhod Ca<sup>2+</sup>-indicator to monitor the activity of the neuronal network following light excitation. We stimulated 11 DIV neurons with light spots ranging from 1 single cell excitation up to 6 neurons. The excitation was carried out using 45 pulses of 20ms at a frequency of 3Hz (Figure 5A) and images of the X-Rhod indicator were obtained with 1.5 Hz frequency 1 minutes before and 2 minutes after stimulation with a 20X objective and without cropping of the field of view. ROI image analysis allows for study of Ca<sup>2+</sup> activities in neuronal

bodies throughout the whole field of view.

The same analysis performed on the ROIs' signals, can be applied for each pixel of the acquired frames: in this way it is possible to create a map of the  $\Delta F/F$  values got in all the pixels' calcium traces, obtaining a "snapshot" of the Ca<sup>2+</sup> responses of the entire network (Color map, Figure 5B). As a first analysis, we evaluated the distance from stimulated neurons and the neurons responding in the field of view. We calculated the distance among the centroid of the

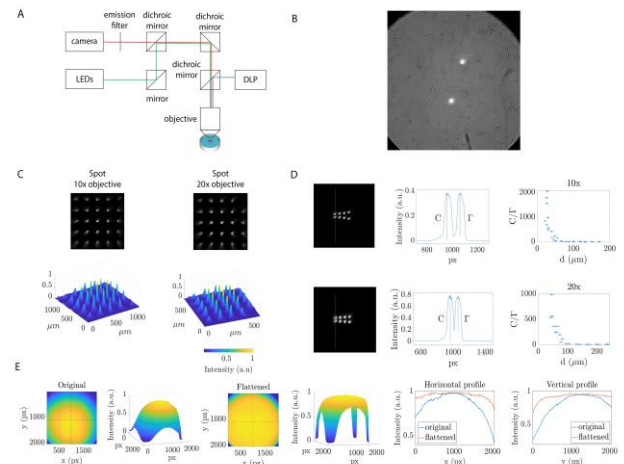


**Figure 4:** (A) Schematic representation of the setup (not in scale): the sample can receive light from the LEDs (Light Emitting Diodes) for the imaging and from the DLP (Digital Light Processor device) for optogenetic stimulation. (B) A possible 2 spot pattern created with the DLP with 20x objective, selecting 2 single neurons in a neuronal network. (C) Light patterns on the sample plane used during the experiments: spot patterns with the 10x and the 20x objective, represented as acquired by the camera and elaborated in 3D. (D) Example of the study on the minimum distance between two spots in the case of the 10x and 20x objective, respectively: the profiles along the blue line are studied, and the C and  $\Gamma$  values are computed. The two spots can be considered independent when the ratio  $C/\Gamma$  arrives at saturation. (E) Representation of the original light distribution on the sample plane in the case of whole FOV illumination, and the flattened distribution obtained after correction. In blue and red are highlighted the cut lines on which the horizontal and vertical intensity profiles are obtained.

spot-illuminated cell and the centroids of all the neurons that responded in the field of view, we normalized the  $\Delta F/F$  values for the maximum value recorded in the FOV and we plotted them in function of the respective distance from the spot, after averaging the values with a binning of 20 units. The results for 2 and 6 spots are shown in Figure 5B. For 2 spots data, responses were stronger near to the excited neurons and decrease about 600 px (195 μm). Since in the field of view a second spot was present, the value increases again: in average the 2 spots were about 1050 pixels distant. Considering this value, also the second slope confirms that neurons communicate until about 195 μm. When a 6 spots excitation is performed, the curve is flatter: since more neurons are simultaneously excited, it is no more possible to distinguish the effect of the single spots.

The histogram in this case reaches the gaussian shape that simply represents the average distribution of the distance between all the neurons in the culture.

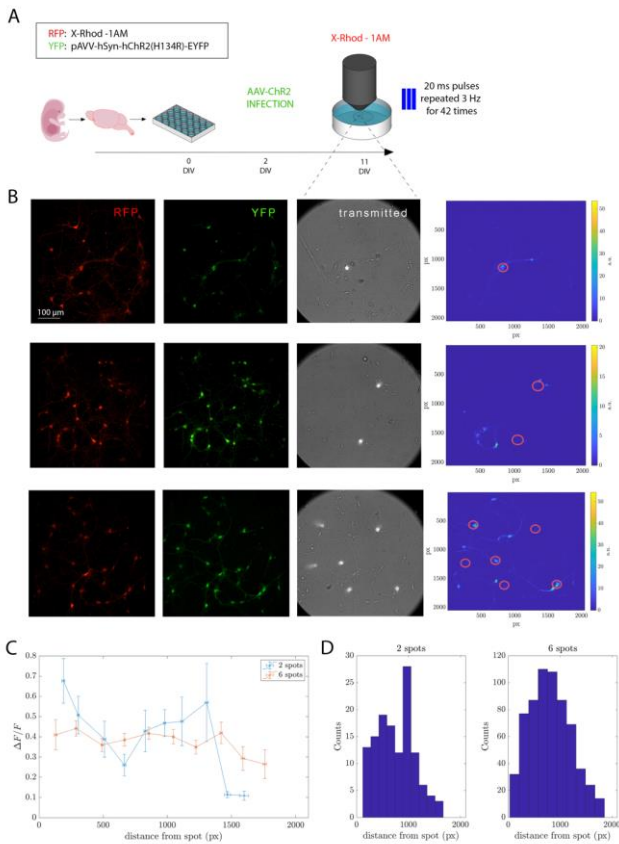


**Figure 5:** (A) A schematic timeline of the experiment, from cell preparation to light excitation. (B) Example of 1, 2 and 6 spot excitation showing X-Rhod expression (RFP), Chr2 infection (YFP), spot stimulation (transmitted) and the pixel by pixel analysis. (C)  $\Delta F/F$  of the responding and not excited neurons in function of their distance from the spot, in the case of 2 or 6 spots. (D) Histograms represent the number of responding neurons at a given distance from the spots, in the case of 2 and 6 spots.

Since the memory engram is formed by a subset of neurons that are stimulated by a specific stimulus during learning, we used the expression of the immediately early gene (IEG) c-fos, an endogenous marker of neuronal activity, as a read-out to designate neurons contributing to the engram ensemble. Cortical Chr2 expressing neurons were spot stimulated with a light pattern known to induce LTP (10 trains of 13 pulses at 100 Hz, repeated at 0,5 Hz) and immunoassayed 60 min later for c-fos expression. To analyze the number of cells expressing c-fos, we set a threshold as the average of c-fos fluorescence intensity of non-stimulated neurons (indicated as out FOV in Figure 6) plus the standard deviation. All neurons overcoming this threshold were accepted as c-fos positive (c-fos+). To test the correlation of c-fos signal with LTP spot-light stimulation, the percentage of c-fos+ neurons was evaluated in the illuminated cells, the not illuminated cells inside the same field

of view (FOV) and cells far from the FOV (out FOV). The analysis reveals that most stimulated neurons express c-fos confirming that they are part of the engram (Figure 6).

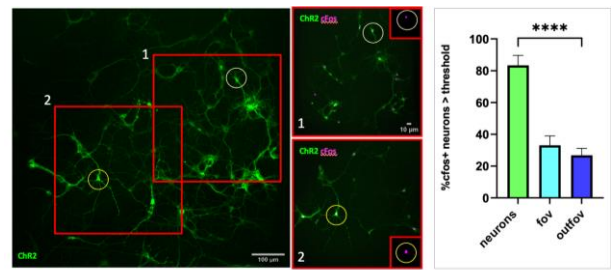


**Figure 6:** Panel on the left shows Chr2 expressing neuronal network visualized with a 10X objective during live experiments. Circular ROIs show the LTP- light spot illuminated neurons. Following immunocytochemistry with a primary antibody targeting c-fos the stimulated neurons were imaged with a 20x objective and showed in ROIs 1 and 2 (red squares). Histogram on the right depict the analysis of c-fos+ neurons in spot-light stimulated cells (neurons), not- illuminated cells inside the same field of view (FOV) and cells far from the FOV (out FOV).

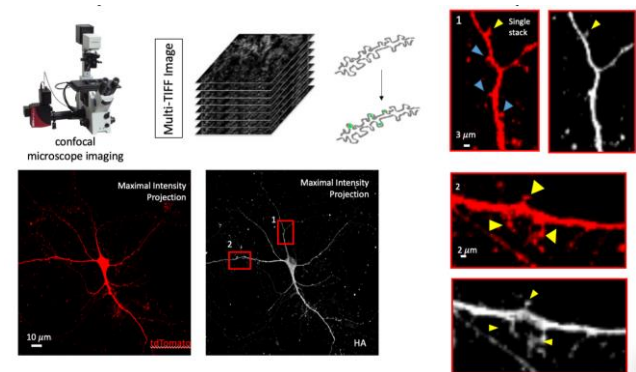


**Figure 7:** (A) Upper panel shows the schematic representation of the confocal analysis. Lower panel shows confocal image (Max intensity projection) of a representative tdTomato positive neurons (red signal) stained for HA expression (white signal) (B) Panels depict 6 times magnification of dendritic ROIS from (A). Ha+ (yellow arrowheads) and HA- (blue arrowheads) are indicated. (C) Histograms depict the percentage of HA+ spines following, 1, 2 and 3 spots light illumination in illuminated neurons, neurons in the same FOV but not- illuminated (FOV) and neurons outside FOV (controls). All data are normalized over the percentage of HA+ spines for control neurons.

To visualize active synapses onto target neurons of interests, we used SynActive (SA), a strategy developed to tag and map the synaptic connections in an input-specific manner (Gobbo et al, 2017). By combining RNA targeting elements with a targeting peptide tag, this innovative method enables to produce cellular tag (HA) precisely at active synapses. This tool allows to unveil the synaptic engram out of the global set of synapses. Spines were morphologically visualized along the dendrites on single confocal z-stack thanks to the expression of tdTomato cellular filler (Figure

7A). For every neuron we manually counted in single confocal z-stack the percentage of spines expressing HA (HA+ spine). Only complete overlapping of tdTomato and HA immunoreactivity was considered as an HA+ spine (Figure 7B). The analysis reveals that after spot-light stimulation (1 spot, 2 spots and 3 spots) the percentage of HA+ spines is significantly higher in illuminated neurons compared to the control cells, suggesting that spots light-LTP stimulation activate specific subset of synapses that are targeted by SA-system (Figure 7C).

Synapses are formed by an essential “third element” complementing the pre- and postsynaptic compartments: the astrocytes. Considering that one single astrocyte can influence thousands of synapses in the rodent brain (and even more in human) these cells appear as ideal candidate for orchestrating the synaptic engram. In *ex vivo* preparation astrocytes gain control over synaptic strengthening and memory upon neuronal instruction (Vignoli et al. 2016; 2021). Starting from this discovery, we will assess in our reductionistic culture system the role of astrocytes in synaptic engram formation (Figure 8).

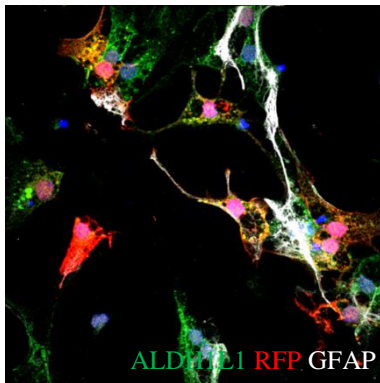


**Figure 8:** Representative image of cultured astrocytes transfected by lipofectamine with GFAP-tdTomato and stained with GFAP, ALDH1L1 and RFP.

#### 4. An animal study of the Astrocytes role in engram formation (Francesca Pischedda, Beatrice Vignoli, Marco Cannonna)

The cerebral cortex is a complex network of neurons that form connections with each other and with other brain regions. These connections allow neurons to communicate and process information, and they can be strengthened or weakened over time through experience-dependent changes known as synaptic plasticity. This is an important process in creating learning and memory circuits, or engrams (Josselyn et al. 2020).

Glial cells, which are non-neuronal cells in the brain, also play a role in learning and memory. They can respond to neuronal activity and release neuroactive molecules (termed “gliotransmitters”) that can affect synaptic activity and modulate plasticity (Haydon and Carmignoto, 2006; Lyon et al., 2022; Nagai 2021). One of these molecules is

brain-derived neurotrophic factors (BDNF) that is secreted by neurons following long-term potentiation (LTP)-inducing electrical stimulation and then recycled in a calcium-dependent manner by astrocytes. This recycling mechanism represent a novel mechanism by which cortical synapses can provide synaptic changes that are relevant for consolidating memory (Vignoli et al., 2016, 2021). Learning and memory can be divided in three stages: encoding (initial learning), storage (maintenance of information) and retrieval (recalling information). One way to study these processes in mice is through the object recognition test (ORT), where mice are exposed to two identical objects and later tested on their ability to recognize one of them as familiar. Using this experimental paradigm, we are now attempting to explore the role of astrocytes in the different phases of memory.

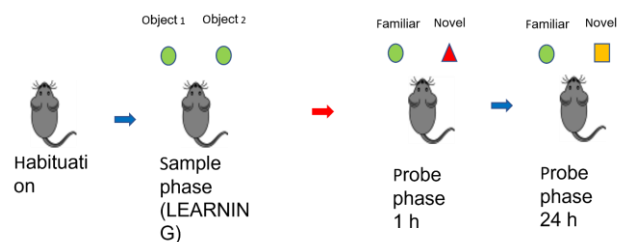


**Figure 9:** Schematic diagram depicting the behavioral paradigm for ORT

#### 5. Modulation of neuronal hyper excitability in epilepsy using optogenetics tools and photonic circuits (Seyedeh Yasaman Heydari)

Epilepsy is a chronic brain disorder characterized by an unpredictable recurrence of seizures. These epileptic seizures are categorized as either focal or generalized. Several different cognitive and emotional dysfunctions can manifest depending on the area of the brain that is affected by epilepsy. The names of the anatomical areas implicated in epilepsy are used to categorize the disorder, such as temporal, frontal, parietal, and occipital-lobe epilepsy. The prevalence of epilepsy is remarkable as includes 1% of the world population. To modulate neuronal activity, conventional medicines are intermittently prescribed regardless of the accurate time of the emergence of the seizure. But nearly 30% of epileptic individuals exhibit drug resistance to all anticonvulsant medications. Moreover, Sudden Unexpected Death in Epilepsy (SUDEP) is one of the deadly side effects of epilepsy that can happen to epileptic patients without specific neuropathological diagnostic characteristics. Additionally, people with long-term focal or partial seizures are more prone to develop malignancies linked to long-term epilepsy (LEAT). To overcome these problems Prof. L. Pavesi newly designed a Neuromorphic photonic circuits chip (Dept. of Physics, the University of Trento in the BACKUP project). This hybrid photonic chip is made up of interconnected optical microring resonators

(MRRs) and waveguides to compute and respond to the aberrant electrical activity of the neurons by optical stimulation in a closed-loop way. To reach this goal, we plan to modify neuronal hyperexcitability in vitro through light stimulation generated by the digital light processor (DLP) in a closed-loop manner. Multi-Electrode Arrays (MEA) recordings are a feasible and reliable system, and provide valuable and precise information about the aberrant electrical network performance of neural cultures. Kainic Acid used for enhancement of neuronal culture excitability. For tracking changes in electrical activity, we performed one-hour continuous recordings with MEA. We began recording 10 min before adding KA (5 $\mu$ M) and continued for 50 min after KA administration. Before that, we did the test with water as a control test. With this protocol, we detected an increase in the number of spikes in compared to baseline (Figure 10, left). Adding water did not show significant changes in spike number in compared to baseline (Figure 10, right).

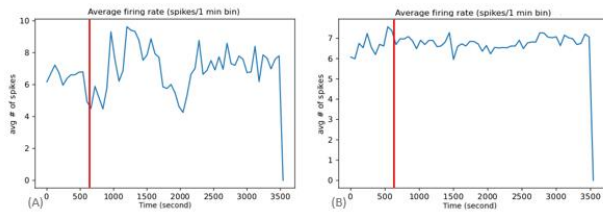


**Figure 10:** Cellular electrical activity throughout a continuous one hour period. The red line shows the moment that the culture receives KA (A) and water(B).

For Setting up DLP system to stimulate neurons with high spatial resolution, we infected the cultures in 3DIV with the viral vector pAAV-SynChr2 (H134R)-YFP to express channelrhodopsin. This channel rhodopsin known as excitatory Channelrhodopsin2 (Chr2) depolarizes neurons through activation of the inward Na<sup>+</sup> and Ca<sup>2+</sup> ion currents and K<sup>+</sup> outward current. Chr2 activation induces action potentials in cultured neurons therefore it is a good candidate to evaluate the neuronal response to light stimulation.

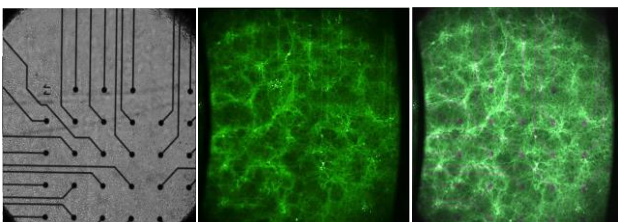


**Figure 11:** pAAV-HSyn Chr2(H134R)-GFP transaction. Neuronal cultures in MEA chip, expression of GFP tag in the culture, merged

Then we employed wide-field light stimulation for the initial tests in this section to measure and confirm how culture responded to light; results showed a clear neuronal

activation following light stimulation at the optimal wavelength for Chr2 activation (Figure 12).

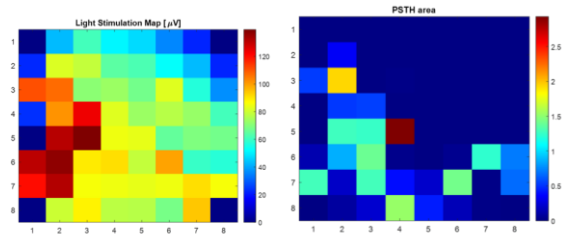


**Figure 12:** Response of the MEA chip to wide-field stimulation. Plots show the response of each electrode according to voltage changes (left), and the mean number of spikes in post stimulus time histogram (PSTH, right).

Next we limited the field of stimulation to an electrode and repeated the trial to prove that we are in the position that we can stimulate the culture with high spatial resolution and track the consequence of this stimulation on the related electrode (Figure 13).

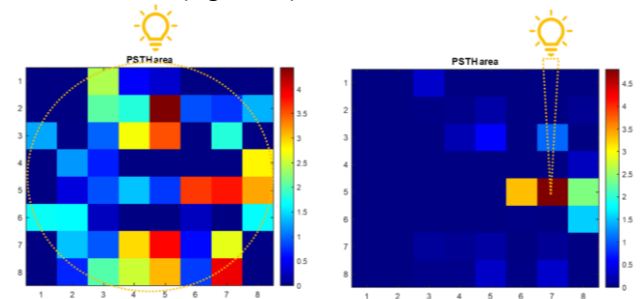


**Figure 13:** Map of the complete response of each electrode to optical stimulation. Plots show the mean response of each channel to wide-field stimulation (left) and a specific channel stimulation(right).

With this arrangement, the next step is to suppress the chemically generated hyperexcitable neuronal culture network. To reach this aim, we will use green light stimulation in the cultures infected with viral vector pAAV-CamKII-ArchT-GFP. This viral vector led to neurons expressing Archherhodopsin. Archherhodopsin (Arch) in the presence of 565nm light pumps out H<sup>+</sup> from neurons, thus inhibiting neurons. To launch the closed loop system, MEA will rapidly detects seizures then this data would be used as feedback for producing proper light impulses that can open the ArchT channels so it can suppress the abnormal activity of the epileptic neurons.

## 6. Characterization of a photonic chip designed for localized neuronal excitation (Clara Zaccaria)

In the last years, we worked on the design and characterization of a photonic chip with grating scatterers properly designed to create light spots on the surface of the chip, with about 10  $\mu$ m diameter. The goal is to optogenetically

excite ChR2 expressing neurons laying on its surface. The chip has grating couplers as inputs and custom designed grating scatterers as outputs. The grating couplers inputs were properly aligned and fixed to a 34-fibers fiber array, to deliver the light to all the grating scatterers distributed along the chip architecture. Before performing biological experiments with neurons laying on the surface of the photonic chip, the light scattered from the gratings was characterized and compared with the simulated distribution. For the sake of this characterization, the chip with its fiber array was fixed in a package suitable to host the neurons and their living solution, as during the experiments.

From now on, we will refer to this system of the chip+fiber array inside the Petri dish as package. The whole system is shown in Figure 14. The fibers of the fiber array (blue ones in figure) end in an array of connectors in which the input laser fiber can be inserted. Multiple inputs can be used, taking advantage of fiber couplers (in figure, yellow fibers on the right are coming from a 1x8 fiber coupler). A custom platform was designed to anchor the system to the microscope sample stage.

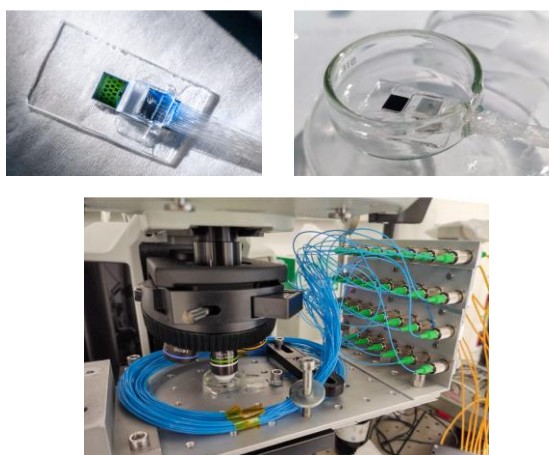


**Figure 14:** Packaging. In the upper part of the figure are shown the system chip+fiber array aligned (left) and the system inserted and sealed in a glass Petri dish (right); in the bottom part is shown the final package, positioned under the 20x water immersion objective.

Once the package is assembled, the scattered light distribution can be characterized, to check the generated light distribution on the surface of the chip (spot). We focused on the efficiency of the system in power delivery as well as on the spatial confinement of the light on the surface of the chip.

The measurements of the power delivery were performed on a package where the fiber array was aligned to the single scatterers matrix side. The power delivered from each single scatterer was collected by a cleaved multimode fiber with 25  $\mu\text{m}$  core diameter, angled by 15°. The total diameter of the fiber was 125  $\mu\text{m}$ . The power collected by the fiber was normalized over an area of about the size of the spot on the surface (78.5  $\mu\text{m}^2$ , 10  $\mu\text{m}$  of diameter) to esti-

mate the intensity received by a neuron. These measurements were performed in air for the sake of simplicity: with water we were not able to correctly see the position of the fiber; the presence of water in principle should enhance the coupling because of a smaller index change in the light path through silica, water, and quartz glass. The values shown in Figure 15 were calculated considering the maximum power of the Cobolt laser (42 mW): the measurements were performed at lower power, measuring both the input ( $P_{in}$ ) and the output power  $P_{out}$ , to get a value of efficiency of the system for each grating. Then, this efficiency was multiplied by the maximum input power available. First, the obtained values' distribution is not even among the different scatterers: this is due to a not perfect alignment and probably to the air bubbles in the glue mentioned before. Anyway, the intensity delivered by most of the gratings is bigger than 1mW/mm<sup>2</sup>, which is a value sufficient to optogenetic excite neurons infected with ChR2.

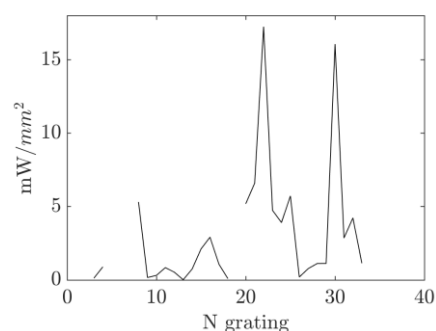


**Figure 15:** The intensity, computed on an area of 10  $\mu\text{m}$  diameter, measured from each scatterer.

To excite selectively single neurons, light must be confined in the desired place, to avoid the excitation of nearby cells. We thus performed the characterization of the distribution of light diffracted by the scatterers, comparing it with the FEM simulations (Comsol Multiphysics). To do so, we analyzed the spots created by the gratings under the microscope, with water inside the Petri dish, to resemble the scattering during the experiment. In Figure 16, an image of the scattered light in far field is shown: 2 spots created by gratings number 24 and 28 in the single scatterer matrix are seen by the microscope.

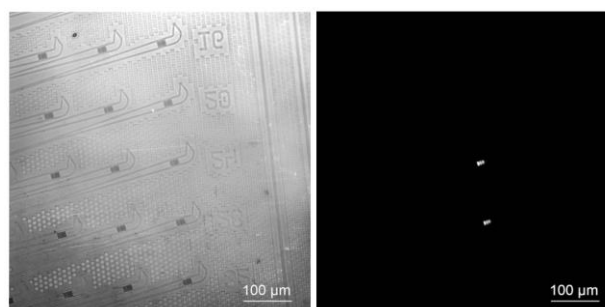


**Figure 16:** Far field scattering. Image taken with the microscope with a 20x objective of the single scatterer matrix (left) and the 2 spots created by grating number 24 and 28 (right).

To study the scattered light in the near field, we performed a stack measurement of the scattered light (on grating number 32) at different  $y$ , acquiring 61 layers around the chip surface plane, with  $1\mu\text{m}$  step. We thus analysed the acquired multi-tiff image in the following way. First, looking at the longitudinal profile of the spot (dashed red line in Figure 17(b)), we computed how the width of the field was changing along the different planes. To define the width, we used the standard deviation  $\Sigma$ , defined as  $\Sigma = [ \langle z^2 \rangle - \langle z \rangle^2 ]^{1/2}$ , where  $p=1,2$ , and  $\langle z_p \rangle = \frac{\int_z z^p |E(z)|^2 dz}{\int_z |E(z)|^2 dz}$ .

We then identified the  $y=0$  plane as the coordinate at which  $\Sigma$  value is minimum (see inset in Figure 17(b)). Rescaling the  $y$  axis of the multi-tiff to this new 0, we could identify the distance of the different planes from the grating, in  $\mu\text{m}$ . In Figures 17(c) and 4(d) the simulated and measured scattered fields in the  $yz$  are shown, respectively. The two maps are similar, considering that the experimental resolution does not let the detection of all the interference fringes simulated and that the numerical aperture does not let the detection of rays scattered at angles larger than  $48.8^\circ$ . Moreover, the chip is not perfectly horizontal, due to the glue layers under it. It is worth to notice that in the measured map the focalization of the intensity is observed between 2 and  $15\mu\text{m}$ , which is where the neurons should lay.

We then focused our attention to the field distribution at  $y=5\mu\text{m}$  (Figure 17(e)). The distributions are quite similar within the above cited limitations. To compare the  $\Sigma$  in these two distributions, we decided to calculate them within a  $z$  axis range at which the measured field is larger than 0.01. Doing so, we are sure that the presence of the not detected lateral fringes will not affect the  $\Sigma$  comparison. The field portions excluded in the calculation are shown in the figure as red. The  $\Sigma$  values got in the two cases are 3.4 and 3.3 respectively. We performed this calculation at different planes between 0 and  $30\mu\text{m}$ , in order to evaluate the divergence of the scattered beam in the two cases. As shown in Figure 17(f), the divergence behaviors are comparable. Then, we checked the spot reconstruction (Figure 18(a)): also in this case, the measured spot resembles well the expected one, with a dimension of about  $10 \times 8\mu\text{m}$ . Also, their profiles along the  $x$  direction match well (Figure 18(b)). All considered, the realized aperiodic gratings work as predicted by the simulations and can focalize the light in the desired planes as expected.

To perform the experiments, neurons are needed to be laying on the surface of the photonic chip. This can be obtained in two main ways: growing the neurons directly on the chip-inside the package or grow the neurons on glass coverlips and locate the cells on the chip just at the moment of the experiment. The first method has the main advantage that the cells will be in direct contact with the chip's surface as supposed during the grating scatterers' design; however, growing cells directly on the package

means that more packages must be available to replicate the experiments, they must be properly sterilized and kept in the incubator, with the inevitable deterioration of the materials.

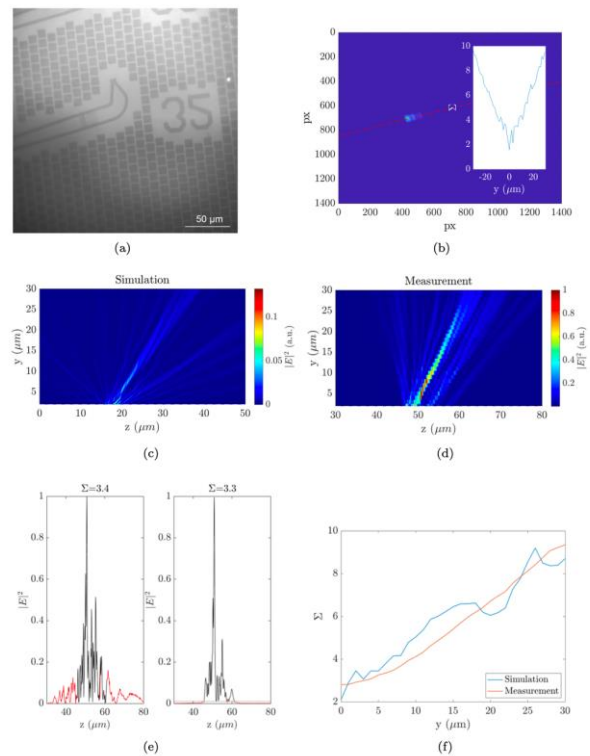


**Figure 17:** Near field scattering. (a) The grating on which the spot acquisition was performed, with a 60x objective; (b) One plane of the analysed image acquisition: the red line is the  $z$  direction considered in the analyses. The inset shows how  $\Sigma$  changes along the acquired planes; the minimum was fixed as plane  $y=0$ . (c) and (d) are the normalized scattering maps obtained in the simulation and in the measurement, respectively. (e) Field profiles along  $z$  in the simulated case (left) and in the measurement (right). Red portions are the one excluded in the computation of  $\Sigma$ . (f) comparison between the  $\Sigma$  values dependence along  $y$  direction.

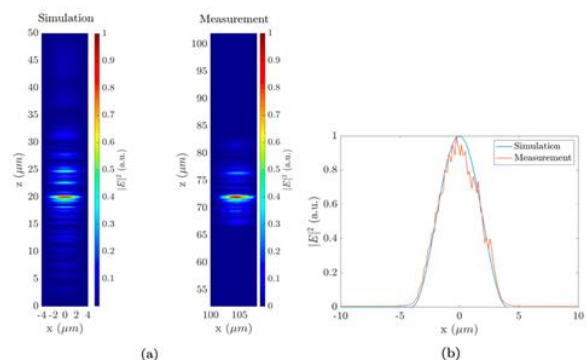


**Figure 18:** Near field scattering. (a) The normalized maps of the spots obtained in the simulation and in the measurement. (b) Comparison of the spot profiles along the  $x$  direction.

The second method indeed let the usage of more coverslips with the same package, saving experimental time and material; the counterpart is that if the neurons are not directly

in contact with the chip surface, the light intensity will be lower than in the optimized plane (chip surface): considering the coverslip thickness, the excitation intensity will be reduced to its 8%. A possible solution could be to position the coverslip upside down, with the neurons directly facing the chip's surface. All these trials are currently on going, to successfully excite neurons with the photonic chip.

## 7. Neuronal networks: in-vitro measurements, characterization and modelling (Ilya Auslander)

### 7.1- Measurements of electrophysiological signals using microelectrode array (MEA) following light stimulation:

In these experiments, we use mice cortical cells, expressing ChR2, plated on a MEA chip. The electrophysiological signals were recorded using MEA-2100mini system of Multi-channel Systems GmbH (MCS) (Fig. 19). The microelectrode array chips used in our experiments were 60MEA-200/30iR-Ti-gr by MCS, which are chips with 60 titanium-nitride electrodes embedded in glass and surrounded by a glass ring. The electrodes are of 30µm diameter, where the horizontal and vertical spacing between each pair of electrodes is of 200µm.

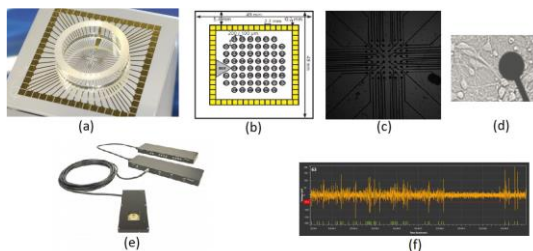


**Figure 19:** MEA system. (a) MEA glass chip, containing the electrode array. (b) Electrode array scheme. (c) A microscope image of the array. (d) A close-up of an electrode surrounded by cells. (e) The electronic system (MCS MEA-2100mini): including headstage, amplifier and interface board. (f) Signal acquisition and spike detection performed on MCS experimenter software: close-up on one of the channels.

The light stimulation source we use is a digital light processor (DLP). The schematic of the experimental setup is depicted in Fig. 20 and a photo of the setup including the MEA, DLP and microscope is shown in Fig. 21.

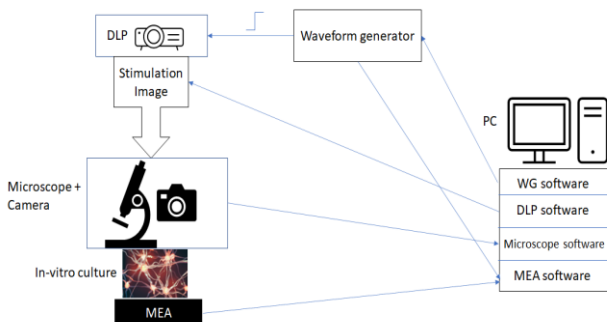


**Figure 20:** A scheme of the experimental setup.

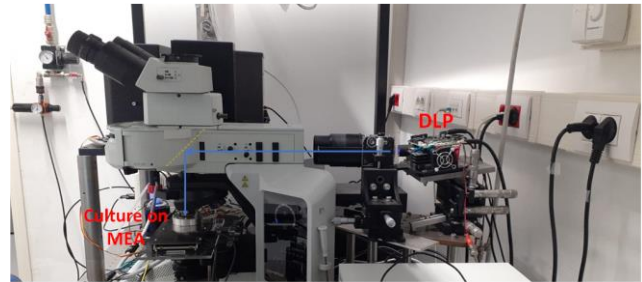


**Figure 21:** The principal part of the experimental setup used in the optogenetic experiments. Patterned light from the digital light processor (DLP) is directed and focused via microscopy system on top of the neuronal sample located on a microelectrode array (MEA) which measures the response of the culture.

Our experiments included spontaneous activity recordings between 10 and 15 minutes. These recordings were performed to evaluate the performance of each culture in terms of spike and bursts rates. Later, we also used this data for the modeling part. In addition, we tested each culture for response to optical and electrical stimuli. With the detected spike trains, we implemented burst detection and network burst detection algorithms, similar to which can be found in literature. For the analysis of light-evoked activity (as well as electrically evoked), we analyzed the response of the network with post-stimulus time histogram (PSTH). Figure 22 shows an example of analyzed electrophysiological data.

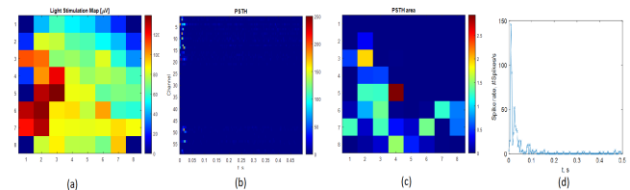


**Figure 22:** An example of MEA measurements analyzed data in a light stimulation experiment. (a) Map of photo-electric response of the electrodes following illumination, which (to some extent) describes the illuminated area on top of MEA. (b) Post-stimulus time-histogram (PSTH)- indicates the neuronal response to light stimulation for each channel of the MEA.  $t=0$  is the stimulus time (c) Map of the PSTH area at each electrode- describes the total neuronal response of the network. (d) PSTH of one of the channels.

We tested the ChR2 expressing cultures and the signal analysis in a response to optical stimulation, using the DLP as the light source. The stimulation temporal pattern was as following: the light pulse length was 20 - 40 ms and the period of stimulation sequence was 0.5 - 2s (0.5-2 Hz frequency); in total we applied 300 pulses in each recording. We tested the response of the network, both for wide-field illumination (i.e., under the field-of-view of the optical system), and illumination of a smaller spot (of a few up to a few tens of microns in diameter) around a small population of neurons. Figure 22 shows experimental results of the neuronal response to light stimulation both for spot and wide-field illumination. These experiments demonstrate the responsiveness of the culture to light following ChR2

infection and also the network connectivity, when stimulating locally in one part and recording a response in other parts of the network.

We then attempted to demonstrate formation of long-term potentiation (LTP) using light stimulation and measuring the response with microelectrode array (MEA). The method of these experiments was to test the response of the culture to light stimulus, before and after a localized tetanic stimulus (high-frequency) stimulus, which induces changes in the synaptic compounds and as a result affects the connectivity among specific circuits, which were potentiated. The test stimulus could be executed as both, in wide-field illumination (almost all over the electrode area), or as a localized spot illumination. The local changes in response between pre- and post- tetanic phases can indicate on synaptic potentiation (or depotentiation) related to some of the cells. The quantitation of the response of network’s response is done by calculating the area under PSTH curve; and the change in the response (efficacy) for each channel is evaluated as:

$$\Delta = \frac{A_{post}}{A_{pre}} - 1$$

where  $\Delta$  is the efficacy measure per each electrode and  $A_{pre/post}$  is the PSTH area (a measure of the response) pre/post the tetanic treatment. Figures 23-25 show the experimental protocol and some preliminary results of this study.

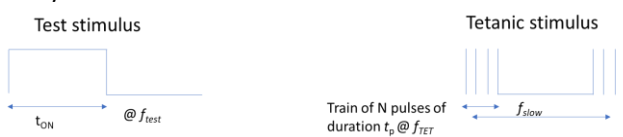


**Figure 23:** Temporal patterns of light stimuli used in experiments: Test stimulus- used to measure the response of the culture; Tetanic stimulus (high frequency)- used to induce potentiation of synaptic connections in the neuronal cultures.

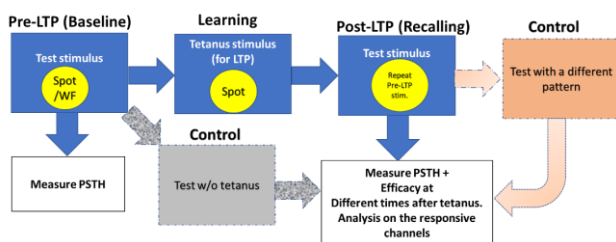


**Figure 24:** Experimental protocol of LTP test.

### 7.2-Modeling and simulation of the biological neuronal network using artificial-neural network:

In this part, we have developed an AI model based on reservoir computing approach, which is able to simulate the response of the neuronal network under test. The model is trained with preprocessed electrophysiological signals recorded on microelectrode array (MEA) system, decodes the spatio-temporal patterns of the recorded signals (spikes) and obtains a macroscopic structure of the culture which is

being tested.

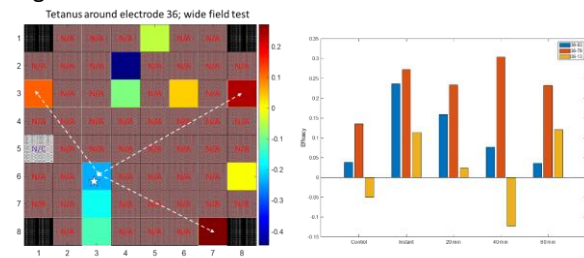


**Figure 25:** An example of LTP experiment result: The tetanic stimulus was applied around electrode # 36 (marked with a star), and the test stimulus was applied in a wide-field illumination. A change in the response is measured between the pre-and post-tetanic phases at the different electrodes. Left: the change in the response for each of the electrodes (N/A- not analyzed- due to low response; N/C- not connected). Right: The change of the response in specific connections at different times after the tetanic stimulation.

We consider a network where each node corresponds to one MEA site (or electrode). Each electrode samples the electrophysiological signals from the neuronal network resulted from the activity of the neuron ensemble (may consist of up to a few tens of neurons) found in its vicinity. We hence define the domain of the MEA measurement as the macroscopic domain, which is described by the network in question, where the real neuronal structure which is sampled by each node will be referred here as the microscopic domain (or the reservoir domain). The data unit which is contained in each of these nodes is a sample of the electrophysiological signals expressed in the instantaneous spike-rate measured in a specified time window. By “data unit” we refer to a set of data sampled at the network nodes in a definite time window, which contains information on the status of the network, with a memory on the previous time steps, and the ability to predict the next step accordingly. The time window is determined by a characteristic rate of the network, which can be obtained, for example, by analyzing for example the inter-burst interval (IBI) histogram. This unit of time is dependent on many properties of the network such as neuron density in the culture, age of the culture and others, and it characterizes the signal integration time of each node.

We then consider the fact that each node in our network represents a complex neuronal signal processing unit. It arises from the fact that typically every electrode of MEA is surrounded by number of neurons (as shown in Fig. 26). The morphology and functionality of each of these microcircuits embedded in each node of the macro network cannot be easily obtained from the electrophysiological measurements of standard MEA systems. Also modeling of such neuronal structures is not an easy task and has been studied for decades, with numerous models for different scales of dimensions and time, no strong consensus however is achieved about the authenticity of these models. For the purposes of our simplified model, we would like to treat

each of these neuronal circuits as a black box, where the morphology and functionality are not known but assumed to be reasonably random. We then assume that the signal at each node is transformed into a higher dimensional domain with arbitrary connections, representing the micro-neuronal circuit. In this high-dimensional domain, the transformed input vector encounters a functional layer which carries memory on previous time-steps. This memory represents the short-term synaptic plasticity and the function represents the non-linearity of the neurotransmission. Following this step, the signals recombine back to the macro-domain through coupled connections between each micro-circuit and each node of the macro-network, forming a new state of the network; then the whole process repeats cyclically. This kind of recurrent network is known as Reservoir Computing Network (RCN) and has been widely studied.

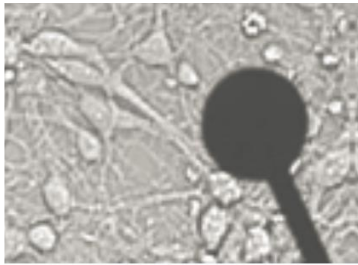


**Figure 26:** An image of neuronal culture on top of microelectrode array, a close-up on a single electrode. This image illustrates the fact that around each electrode there is a complex neuronal micro-circuit

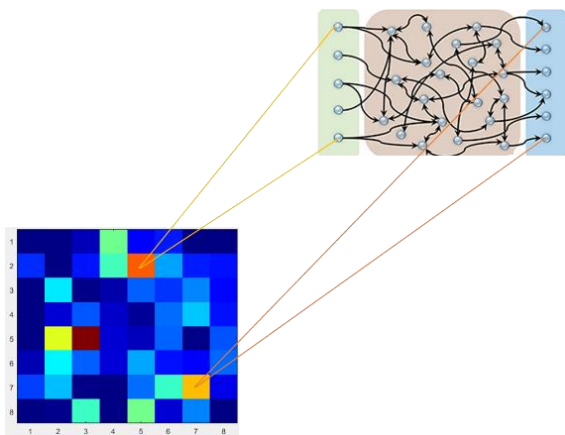


**Figure 27:** A map of MEA measurement. Each pixel in the matrix represents a node of the macrodomain network, corresponds to one electrode of MEA. The color-scale of the pixels represents the instantaneous activity in the vicinity of each electrode (e.g., in units of spikes per second). The inset shows the complex circuit embedded in each node, which is considered in this model as a micro-reservoir network with randomly connected micro-nodes.

The model is implemented on an artificial neural network ANN structure, whose architecture is depicted in Figure 28. For the above structure we implemented the following relations:

$$\mathbf{x}[n] = \mathbf{f}_{NL}(\mathbf{W}_{in}\mathbf{y}[n] + \alpha\mathbf{W}_{res}\mathbf{x}[n - 1])$$

and,

$$\mathbf{y}[n + 1] = \mathbf{W}_{out}\mathbf{x}[n]$$

here  $\mathbf{x}[n]$  and  $\mathbf{y}[n]$  denote the state of the reservoir and the macro network, respectively, at each time step  $n$ ;  $\mathbf{f}_{NL}(x, y)$  is a vector-valued non-linear function, whose output is dependent both on the previous reservoir state and the current input from the network;  $\mathbf{W}_{in}, \mathbf{W}_{res}$  and  $\mathbf{W}_{out}$  are matrices of weights of the input, reservoir and output layers, respectively and  $\alpha$  is the memory parameter.

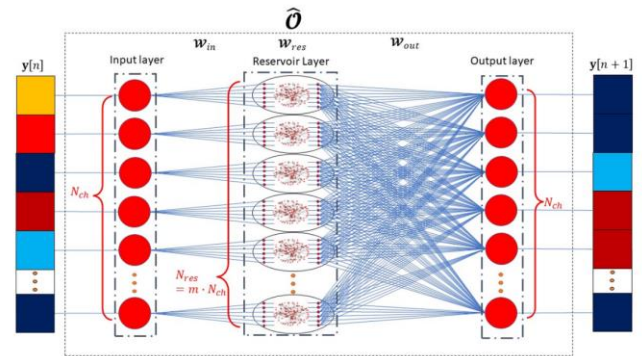


**Figure 28:** The ANN structure of the model

In this scheme, the training is applied only on the output weights of  $\mathbf{W}_{out}$  matrix, and since the relation in of the output layer is linear, it is sufficient to train it with linear regression. The training data is collected from the preprocessing of MEA measurements, where it is arranged as time-binned spike trains (spike-rate coded information) over events of network bursts (spontaneous activity) or post stimulus time windows (evoked activity). The diagram describing the data collection, training and validation of the model is shown in Figure 29.

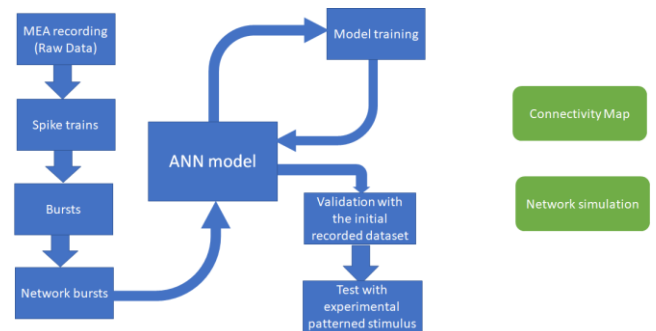


**Figure 29:** A diagram describing the modeling procedure

After the model is trained (and after some mathematical manipulations) it is possible to describe the given culture in terms of macroscopic connectivity (as a graph model) between the nodes of the network. In addition, it is possible to test this network as a response to various stimuli. Figure 30 shows some of the preliminary results obtained from the model, where we produce the macroscopic connectivity map and simulate the response of a given stimulation with comparison to an experiment where localized

light stimulation was applied with the DLP.

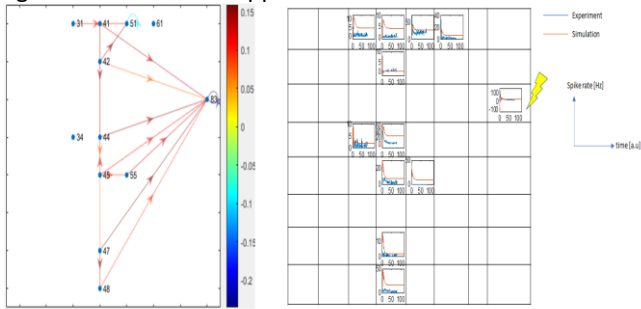


**Figure 30:** Results obtained from the ANN model. Left: Connectivity map describing the weighted connections between different nodes, where each node represents an electrode in MEA measurements, which in fact describes the neuronal circuit around that electrode (The Map shows connections of weights above a specific threshold). Right: Simulation of the network response to stimulation at electrode #83 and comparison with the experimental response (to a light stimulation).

### 8. Signal distortions compensation using an integrated photonic neural network (Emiliano Staffoli, Mattia Mancinelli, Davide Bazzanella)

Modulated optical signals propagating in fibers are affected by distortions induced by linear effects, among which one of the most severe is represented by chromatic dispersion (CD). This alters the shape of the optical pulses traveling in fiber, generating an intersymbol interference between adjacent bits and causing a loss of information between the transmitter and the receiver. This in turn implies the necessity of distortion compensation along the propagation path. To compensate or correct for CD, several types of equalization techniques have been introduced, among which dispersion compensated optical fibers and Bragg gratings are the most diffused ones. An alternative solution is proposed by the University of Trento with the ALPI project, which intends to use integrated Photonic Neural Networks (PNNs) to recognize and compensate distortions in optical signals. The advantages in the adoption of this technology derive from operating the corrections directly on the optical sequence, drastically reducing the latency as well as increasing the flexibility of the equalization, which can be learned directly on the deployed link and, therefore, can be easily adapted to optical link variations.

We performed some tests on a 4-channel delayed complex perceptron (DCP), using the experimental setup described in Figure 31. The device splits the input signal into 4 channels and uses the combined action of delay lines (spirals) and tunable phase shifters (small blue rectangles) to create a desired interference pattern at the output. The nonlinear node of the PNN is represented by the square modulus  $|E|^2$  applied during the detection process. This working principle has been applied to compensation of

distortions induced by linear effects during propagation in fiber. The action of the PNN aims to recognize these distortions and to provide an effective compensation to restore the original shape of the optical sequence.

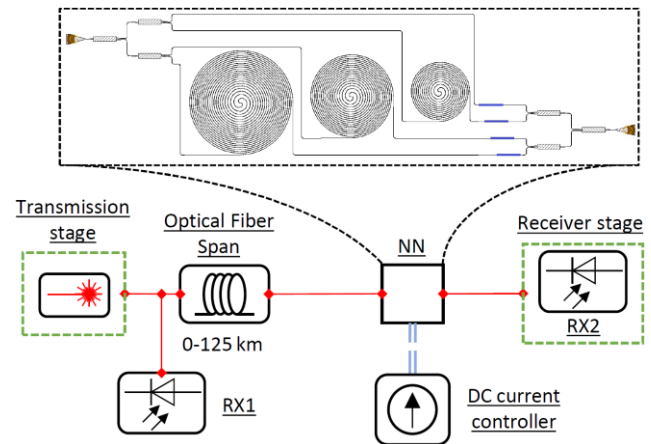


**Figure 31:** Simplified experimental setup. Light is generated and modulated in the transmission stage and then sent into an optical fiber span where it accumulates distortions induced by chromatic dispersion. Then, it proceeds the DCP for optical processing. Two fast photodiodes monitor the input (RX1) and the output (RX2) signals.

The transmission stage produces an optical signal modulated as a Non-Return-to-Zero Pseudo-Random binary sequence at 10 Gbps. The signal then propagates into a fiber span, whose length has been varied from 0 to 125 km. Here distortions are accumulated and then the signal is provided as input to the DCP. The tunable parameters of the perceptron are represented by the 4 phase shifters (heaters), which are driven by a DC current controller. The optical signal is acquired both after the transmission stage (RX1) and after the PNN (RX2). The similarity between the two curves (and thus the goodness of the action of the PNN) is measured the Bit Error Rate (BER), which is defined here as an error counting between the digitized input and output signals, obtained by applying a threshold level to the acquired voltage curves. We tested two different training algorithms, namely the Particle Swarm Optimizer (PSO) and the Adam algorithm, this consisting in a gradient descent provided with memory. The whole experimental procedure was performed in parallel with numerical simulations.

The delayed complex perceptron provided effective compensation of distortions induced by linear effects during fiber propagation. The major benefits deriving from the implementation of the device were observed for long fiber spans, where the distortions to be corrected are more evident. An example of the results of the compensation process is reported in Figure 32. It is possible to appreciate how the PNN manages to reduce the effect of intersymbolic interference, increasing the contrast between bits expected as 1s and 0s, and thus the BER.

The performed training procedures highlighted the features of PSO and Adam algorithm as function optimizers. The former spends more time for the research, ultimately providing an exploration of a wider region of the space of configurations looking for absolute minima of the loss function. The latter is more rapid, but limited by the possibility of ending the research at a local minimum.

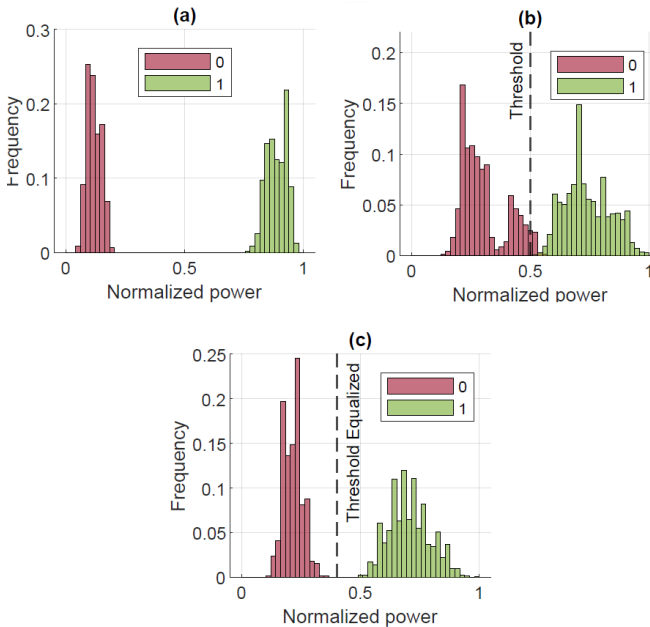


**Figure 32:** Results of the training procedure performed with PSO for 125 km fiber link. (a-c) Distribution of bit values expected as 0s or 1s in the input signal (a), distorted output (b) and equalized output (c).

An 8-channel delayed complex perceptron has been tested on chromatic dispersion compensation too. The new structure is equipped both with phase and amplitude weights in each channel, conferring more versatility to the structure. The higher level of complexity of the new PNN allows dealing with more demanding problems, as the equalization on a 40 Gbps PAM4 signal propagating in a 50 km fiber. With the new modulation format, the loss function provided to the PSO for the training aims to create the maximum relative separation between the distributions associated with the expected optical levels (i.e. the maximum contrast between levels). The corresponding results are reported in Figure 33. In the input signal, 4 distributions appear, one for each level of modulation. The transmission quality in terms of distribution separation at the input is limited by the instruments in the transmitter. When the DCP is not included in the transmission line, all the information at the output is lost, with no clear distinction between the 4 levels. This is due to the effect of the intersymbol interference generated by the CD. On the contrary, with a trained DCP inserted after the transmitter, the 4 distributions return to be equal to the input one.

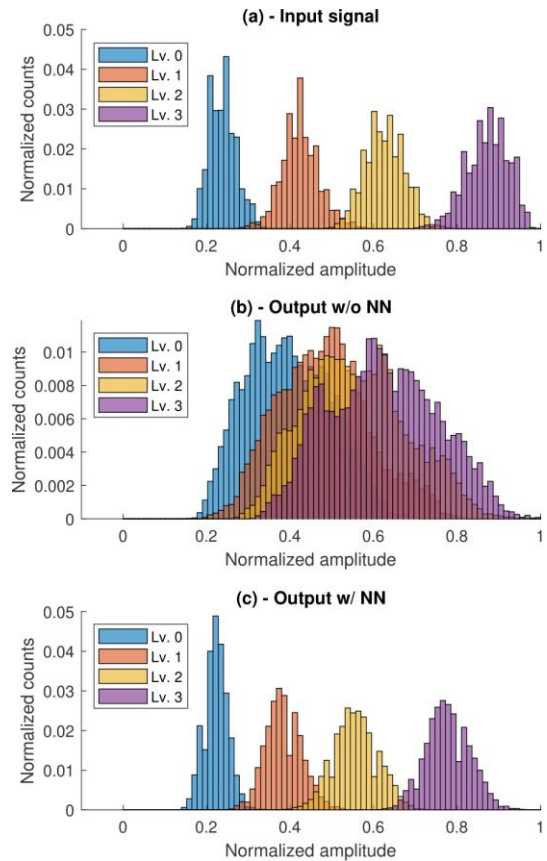


**Figure 33:** Distributions of optical levels (a) in the input signal, (b) at the output after the uncompensated propagation in a 50 km span, and (c) with the corrective action of the PNN.

## 9. Time-delay reservoir computing with a single microring resonator: experiment (Giovanni Donati)

Here an experimental realization of a time-delay Reservoir Computing is realized. The single node of the structure is a delayed-ring resonator, realized by coupling a microring resonator in add-drop filter configuration which is integrated on a silicon chip, to an external optical feedback realized via an optical fiber. Based on numerical simulations performed the previous year, the strength and the phase of the feedback signal are key parameters to be controlled while solving a task. Thus, along the feedback line a gain medium (Semiconductor Optical Amplifier, SOA) is used for both compensating the coupling losses between the grating couplers and the fiber ( $\approx 5$  dB each one) and tuning the optical power (strength) of the feedback signal. A phase shifter is also incorporated through a piezo-fiber stretcher, externally driven by an Arduino Mega.

The dynamical response of the structure to a given input task is collected from the drop port of the microring. An opto-electronic controller that was developed the previous year and now adapted to this system, is engaged for the stabilization against thermal, vibrational and photonic noise.

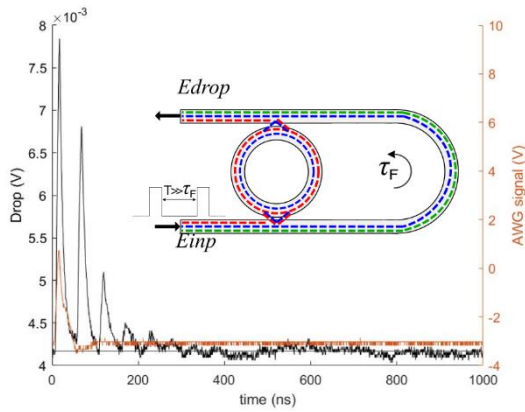


**Figure 34:** Optical echoes (black curve) following an input optical pulse (orange curve) measured at the drop port, when light is partially resonant to the microring cavity (blue path in the inset). When it is perfectly resonant (red path in the inset) or completely out of resonance (green path in the inset) no fading memory is observed.

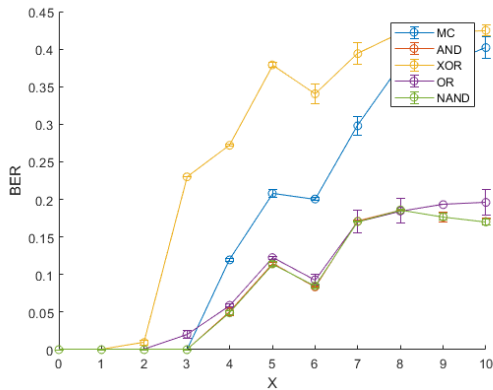


**Figure 35:** Summary of results obtained in two-bits delayed binary tasks, in terms of the Bit Error Rate (BER), the ratio of misclassified input bits over their total amount. The tasks are evaluated between the current bit and a bit injected  $X$  steps in the past, exploiting the dynamical response to only the current one.

The computational properties of the system for time-delay reservoir computing are first studied by measuring the number of delayed copies that follow the injection of an input optical pulse and then probing the delayed-microring in two-bits delayed binary tasks. These tasks include the Boolean XOR operation, due to the nonlinear separability it requires, and are encoded as a PRBS at the input layer by modulating in intensity the CW light emitted by an infrared laser. The experimental parameters scanned are the detuning between the input and the microring resonance wavelengths, the feedback strength, the feedback phase and the average input optical power. An example of the observed system's fading memory is reported in Figure 34, and shows that light is indeed able to iterate multiple times the microring-feedback loop, thus providing memory capabilities to the system. The binary tasks are performed with

different number of virtual nodes (3 and 7), realized by varying the length of the feedback fiber. The best performance obtained when using 7 virtual nodes are summarized in Figure 35 and highlight how the XOR operation can be solved when considering the current bit and up to two bits in the past. The system clock frequency is here dictated by the delay provided by the feedback, that for 7 virtual nodes is  $\tau_F=88$  ns.

The number of virtual nodes is here strongly limited by the Arbitrary Waveform Generator (AWG – 500 MHz) used to encode the masked optical input information. Faster AWGs allow for higher input rates and reduced feedback lengths, while maintaining the same number of virtual nodes, or higher. Following this reasoning, an updated and fully integrated version of the delayed-microring has been designed, relying on two microring resonators coupled in a scissor geometry, each one equipped with a p-n junction, and coupled to a waveguide-based feedback. The structure is also provided of multiple output channels to further improve the number of available virtual nodes, via spatial-time multiplexing.

## 10. A Microring as a Reservoir Computing Node: Memory/Nonlinear Tasks and Effect of Input Non-ideality (Mattia Mancinelli)

The microring resonator (MR) in the nonlinear regime for reservoir networks has been extensively studied within the BACKUP project [BorPP, BazMemNon]. Complex tasks are performed by exploiting the nonlinear dynamics of the MR and a linear regression layer as output.

A single microresonator in the add-drop configuration is used as a reservoir network, implementing virtual nodes through the time multiplexing technique [VirtSande]. The number of virtual nodes  $N_v$  is determined by the bit duration  $T_b$  and the virtual node temporal separation ( $\delta t$ ), i.e.  $N_v = T_b/\delta t$ . The input signal is an optical binary sequence  $\mathbf{I}_N$  of length  $N$ , encoding the logical binaries 0 and 1 with the lowest and maximum optical intensities of a single-frequency pump laser, respectively. The input optical signal is then a sequence of bits  $\mathbf{b}_j^i$ , each of which is composed by a  $N_v$  number of samples  $i_j$ , or virtual nodes:

$$\mathbf{I}_N = (\mathbf{b}_1^i, \dots, \mathbf{b}_j^i, \dots, \mathbf{b}_N^i) \quad \mathbf{X} = (\mathbf{b}_1^{oT}, \dots, \mathbf{b}_j^{oT}, \dots, \mathbf{b}_N^{oT})$$

$$\mathbf{b}_j^i = (i_1, \dots, i_j, \dots, i_{N_v}). \quad \mathbf{b}_j^o = (o_1, \dots, o_j, \dots, o_{N_v}),$$

**Figure 36:** Input and output sequence definition

The output bit  $\mathbf{b}_j^o$  is measured at the output port of the system, i.e. the microresonator (MR) transmitted light is detected and sampled each  $\delta t$  yielding the virtual nodes status  $o_j$ . These output bits are arranged in the hidden nodes matrix where each column  $\mathbf{b}_j^o$  contains  $N_v$  virtual nodes (Figure 36). Then, offline, the RC output  $\mathbf{Y}$  is obtained by simple matrix multiplication of the hidden nodes matrix with a weight matrix  $\mathbf{W}$ , i.e.  $\mathbf{Y} = \mathbf{XW}$ . The reservoir training

is obtained by determining the weight matrix  $\mathbf{W}'$ , which allows predicting the target  $\mathbf{Y}_T$ . This problem is solved by regularized least squares (ridge regression), exploiting the fitrlinear algorithm of Matlab. Here, the regularization parameter  $\lambda$  is defined by 5-fold cross-validation, so that the result of the ridge regression is the matrix  $\mathbf{W}'$  which minimizes the regularized least square error.

The possibility of varying both the frequency and power of the pump laser (control parameters) allows for studying the effects of the MR nonlinear response [BorTher]. This nonlinearity, applied to the input signal, is due to either or both the dynamics of the free carrier population density and the temperature within the MR's waveguides. The pump laser generates free carriers through Two-Photon Absorption (TPA) which, in turn via free-carrier dispersion, generates a blue shift of all the resonant frequencies of the MR. On the other hand, the temperature of the MR increases due to free carrier relaxation and light absorption in the waveguide material. This induces a red shift of all the resonant frequencies due to the thermo-optic effect. The two effects are characterized by different relaxation times and power dependences. Then, depending on the frequency detuning (difference between the pump laser frequency and the MR resonant frequency), the input power and the bit rate, one of these phenomena can overcome the other or both can occur leading to an unstable scenario characterized by a self-pulsing regime [BorTher]. As a result, such nonlinearities that define the connection between the virtual nodes [BorPP], have the potential to provide both the memory capability and the nonlinearity of the reservoir.

The binary tasks studied are the logical operations AND, OR, and XOR which are carried out on the present bit with a bit in the past (delayed task). Here we are going to focus on the XOR task while full details can be found in the original article [BazMemNon].

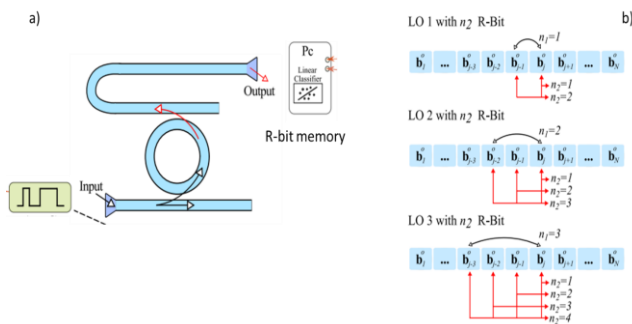


**Figure 37:** (a) Sketch of the MR in the add-drop configuration. (b) Sketch representing the three cases on which we tested the logical operations.  $n_1$  indicates the distance between the bits on which the logical operation (LO) is performed and  $n_2$  is the number of bits provided to the ridge regression in the training procedure. The flow of bits is such that the past bits ( $b^{j-n1}$ ) are processed by the MR before the present bit ( $b^j$ ), i.e. the bit flow is inverted with respect to the time flow which is indicated in the figure.

To explicit the bits on which the operation is carried out, we use the following notation explained in Figure 37(b):

“LO  $n_1$  with  $n_2$  R-bit”, where LO is the logical operation,  $n_1$  is the distance between the bits on which the LO is performed (the present and the past bits), and  $n_2$  is the number of bits, starting from the present one, provided to the ridge regression (the R-bits). Varying the distance between the bits subject to the logical operation allows testing the memory imprinted on the output signal by the MR. We can supply to the ridge regression the current bit only, so that the system must provide the memory to the regression, or we can make all the bits in the operation directly available to the regression. In the last scenario, the attention can be focused on the nonlinearity of the MR imprinted on the output signal.

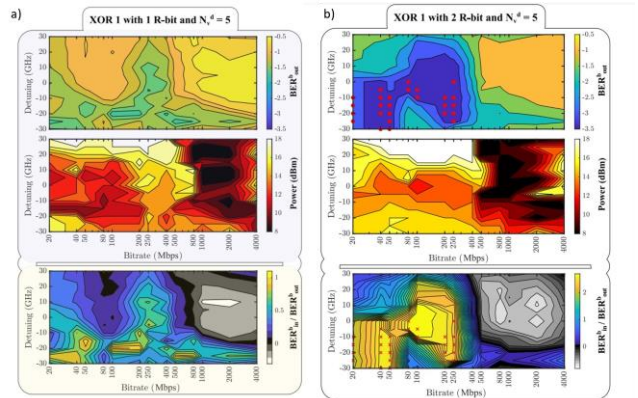


**Figure 38:** Maps as a function of the frequency detuning and input bitrate for XOR 1 with (a) 1 R-bit, (b) 2 R-bit and  $N_v^d = 5$ . (top) BER estimation from the RC network at the power which ensures the best network performances; (middle) the power at which the  $BER^{b_{out}}$  values in the first panel are achieved; (bottom) the ratio between  $BER^{b_{in}}$  and  $BER^{b_{out}}$ . All the values are given in a logarithmic scale.

Figure 38 reports the performances of the RC network as bit-error-rate for task XOR1 with (a) 1 R-bit and (b) 2 R-bit as a function of the detuning and input power ( the control parameters ) and the input bitrate. The first map shows the best value of the BER ( $BER^{b_{out}}$ ) obtained by the RC network with the input power which ensures the best performance. The second map shows the lowest value of input power at which  $BER^{b_{out}}$  is achieved. The third one shows the ratio RB between the BER<sup>b</sup> estimated when the ridge regression is applied on the input optical data ( $BER^{b_{in}}$ ) or on the output optical data ( $BER^{b_{out}}$ ):  $RB = BER^{b_{in}}/BER^{b_{out}}$ . The color code for the ratio RB is given on the map with two different color ranges: one from blue to yellow, and the other from black to white. The first highlights where the MR introduces an improvement of the performance. Specifically, the yellow indicates a better result of the RC network, and therefore, defines the regions of performance improvement given by the MR nonlinearity. The other color range is a gray scale that shows where the results of the RC are worse than barely performing the ridge regression on the input optical data. In particular, the black indicates that RB is equal to one, i.e. the task is solved with the same BER either when the input optical data are processed or when the output optical data are processed, while the gray and white

colors indicate regions in which  $BER_{out}^b$  is worse than  $BER_{in}^b$ . This means that the nonlinear response of the MR does not introduce any advantage but it is only detrimental. For the sake of clarity, all the maps are represented with a logarithmic ( $\log_{10}$ ) scale.

By comparing Figure 38a with Figure 38b it turns out that the RC network is not able to properly handle the 1-bit memory and the nonlinearity required to solve the XOR1 task without errors. In fact, the  $BER_{out}^b$  in Figure 38a is not reaching the statistical limit and the RC network barely solves the task. Instead, Figure 38b shows a large area where the  $BER_{out}^b$  is reaching the statistical limit, a sign that the additional memory provided at the readout to the ridge regression improves the overall performance. There is a trade-off between the memory quality and the nonlinear transformation that limits the MR used as an RC node.

Another important outcome of the study is the role of the non-idealities of the input preparation. The bottom panel, reporting the RB parameter, is meant to identify the condition in which the output performs better than the input. The limited electronic bandwidth and the nonlinearities of the electrical amplifiers that drive the Mach-Zehnder-Modulator required to imprint the input information onto the optical signal can already act as a reservoir before the MR itself. Being the MR a nonlinear system, there are conditions in which the input information is distorted in a useless way to the linear classifier.

### 11. On the modelling of RCN memory: linearized nonlinear microring resonator (Mattia Mancinelli)

Despite its apparent simplicity, the intricated nonlinear effects related to the silicon-on-insulator platform make the MR's dynamics extremely rich. Understanding this complexity is the key to harnessing the platform's potential.

The recent work done within the BACKUP project goes in this direction. We attempted to analyse the single MR system starting from the well-established CMT equations and performing a linearization and stability analysis (LSA). The aim was to understand the kind of memory induced by the nonlinearities. Moreover, the final goal of this approach is to develop a fast and efficient way to figure out the best control parameters to engineer the memory of the single and coupled MRs systems. In fact, the method used up to now relies on a brute-force numerical approach that scans over the control parameters to get an a posteriori estimate of the system memory. High computational time is typically required preventing applying this method on a system based on several coupled MRs.

We started from the system of 4 real-valued autonomous first-order coupled nonlinear differential equations reported in Equation 1, which describes the dynamics of a nonlinear MR as a function of the control parameters, which are the complex input power amplitude  $E_{inc}$  and frequency  $\omega/(2\pi)$  using the complex cavity field amplitude  $a$ ,

the displacement from equilibrium of free carriers concentration and temperature in the ring ( $\Delta N$ ,  $\Delta T$ ). Since the energy amplitude timescale ( $\sim 10$  ps) is much smaller than the free carriers and temperature timescales ( $\sim 10$  ns,  $\sim 100$  ns), we simplified Eq.(1) by setting  $da/dt = 0$  assuming that the cavity field inside the ring is always at equilibrium. Notice that, even under such approximation,  $a$  implicitly depends on time through  $\Delta N(t)$  and  $\Delta T(t)$ .

$$\begin{aligned} \frac{da}{dt} &= -ia(\omega - \omega_0(\Delta N k_N - \Delta T k_T + 1)) - a\left(\gamma_k |a|^2 + \Delta N \gamma_{N_2} + \frac{1}{\tau_l}\right) + i\sqrt{\frac{1}{2\tau_{ex}}} E_{inc} \\ \frac{d\Delta N}{dt} &= \frac{\sigma_N |a|^4}{\omega} - \Delta N \gamma_{N_1} \\ \frac{d\Delta T}{dt} &= |a|^2 (\Delta N \sigma_{T_N} + \sigma_{T_2}) + |a|^4 \sigma_{T_1} - \Delta T \gamma_T, \end{aligned}$$

**Equations 1:** Coupled differential equations from CMT describing the MR nonlinear time evolution

By considering the cavity amplitude field always at equilibrium and by manipulating the first equation in Equation 1, we were able to evaluate  $|a|^2$  as a function of  $\Delta N$  and  $\Delta T$ , reducing the system of 4 real-valued equations into 2 real-valued equations (Equation 2). By relying on numerical methods, we evaluated the equilibrium values of  $\Delta N$  and  $\Delta T$  as a function of the control parameters. Depending on the control parameters, the system allows at least 1, and at most 3 equilibrium points in the  $(\Delta N, \Delta T)$  parameters space. As described in [RefLSA], the LSA consists first in linearizing the approximated version of Eq.1, at one equilibrium point  $(\Delta N_{eq}, \Delta T_{eq})$ , introducing the two implicit nonlinear functions  $F_T$  and  $F_N$ .

$$\begin{aligned} \frac{d\Delta N}{dt} &= F_N(|a(\Delta N, \Delta T)|^2, \Delta N) \approx \frac{\partial F_N}{\partial \Delta N} (\Delta N - \Delta N_{eq}) + \frac{\partial F_N}{\partial \Delta T} (\Delta T - \Delta T_{eq}) \\ \frac{d\Delta T}{dt} &= F_T(|a(\Delta N, \Delta T)|^2, \Delta N, \Delta T) \approx \frac{\partial F_T}{\partial \Delta N} (\Delta T - \Delta T_{eq}) + \frac{\partial F_T}{\partial \Delta T} (\Delta T - \Delta T_{eq}), \end{aligned}$$

**Equations 2:** Reduced differential equations for stationary optical field

It follows that if the system is close enough to an equilibrium point the linearization is accurate and the system obeys Equation 3.

$$\begin{pmatrix} \Delta N - \Delta N_{eq} \\ \Delta T - \Delta T_{eq} \end{pmatrix} = k_1 \vec{\xi}_1 e^{\lambda_1 t} + k_2 \vec{\xi}_2 e^{\lambda_2 t}$$

**Equation 3:** Linearized system

where  $\vec{\xi}_{1,2}$  and  $\lambda_{1,2}$  are the two eigenvectors and eigenvalues of the Jacobian of the linearized system in Equation 2 as a  $2 \times 2$  matrix, while  $k_i$ ,  $i = 1, 2$  are real-valued constants fixed by the initial conditions and  $t$  is the time. By looking at Equation 3, one sees that if at least one eigenvalue has a real part larger than zero ( $\text{Re}(\lambda_i) > 0$ ,  $i = 1$  or  $2$ ), then  $\Delta N$  and  $\Delta T$  diverge from the equilibrium at large times (as long as the eigenvectors have no zero components), thus the equilibrium is unstable. In case both eigenvalues are smaller than zero, the equilibrium is stable with the free carriers and temperature time evolution approaching their

equilibrium value. An imaginary part of the eigenvalues different from zero implies oscillatory dynamics. In other terms, Equation 3 tells us the shape of the system trajectory near an equilibrium point. The eigenvalues are directly related to the system memory since they represent the (complex) decay rates of the dynamics, i.e., the time that the system takes to relax back to its equilibrium point after a small perturbation. Figure 39 reports maps of the second eigenvalue's real part (MHz) as a function of laser-MR detuning  $\Delta\nu$  and input power  $|E_{inc}|^2$  as calculated from LSA theory with superimposed isolines identifying areas of self-pulsing (solid black) and where the system can effectively remember 2 bits in the past when used as reservoir network (dashed red) as calculated from the numerical solution of the differential equations system.

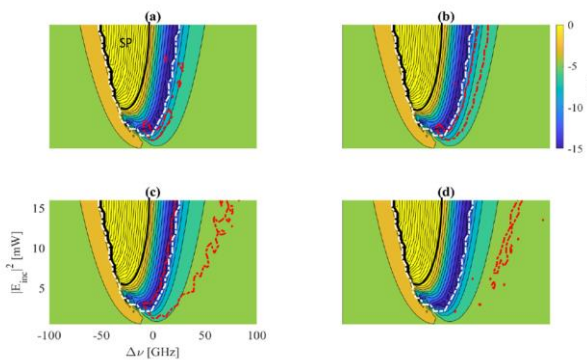


**Figure 39:** Real part of the eigenvalue (frequency) as a function of the detuning and input power: colour bar in MHz. The contours represent (black) self-pulsing region ( $Re(\lambda) > 0$ ), (dashed white) oscillating decay  $|Im(\lambda)| > 0$  and (dashed red) a bit-error-rate for the 2-bit delayed "mem" task equal to 5%. The modulations and bit rates employed are (a) 0.8 – 1.2 and 10 MHz, (b) 0.8 – 1.2 and 9.1 MHz, (c) 0.8 – 1.2 and 5.9 MHz, (d) 0.25 – 2.25 and 5.9 MHz.

Associating just 2 timescales, the FC and Thermal one, to the system is a misinterpreted idea. The nonlinearity makes the scenario anything but trivial. The system can evolve with a continuum of timescales where the maximum memory (inverse of the eigenvalue) can even approach infinity at the edge of stability (solid black line). In this particular case, the available timescales range from 15 MHz to 0 MHz, the edge of stability.

The dashed red line is generated by solving numerically the system dynamic when the input is modulated as a PRBS8 waveform. The output time evolution is then used to extract virtual nodes where the linear readout is trained to solve the selected task. The LSA allows one to get general information on the network dynamics that are also related to its capability to effectively solve tasks.

The LSA allows one to predict the control parameters to have a good memory. In fact, the system can solve the tasks in a region defined by the white line, that is the region where the eigenvalue's imaginary part becomes 0. What emerges is that oscillatory relaxation is detrimental to memory quality. Even the self-pulsing region, perfectly pre-

dicted by the LSA theory (complex conjugated eigenvalues), is forbidden when tasks have to be solved.

## 12. An integrated microresonators array to implement the Extreme Learning Machine algorithm (Stefano Biasi, Riccardo Franchi and Lorenzo Cerini)

Typically, in a neural network, the original information is mapped to a higher dimensional space and is processed by means of non-linear functions. The mapping can be viewed as a linear matrix-vector multiplication with certain weights. In a reservoir computing approach, the weights that make up this large space are chosen randomly, and training occurs only in the readout layer. Among the approaches based on random neural networks, the Extreme Learning Machines (ELM) represent a powerful paradigm. The ELM algorithm was proposed by Guang-Bin Huang in 2006. It consists of applying linear combinations through random weights to map the initial database into a higher dimensional space. A nonlinear infinitely differentiable activation function is applied to that space, yielding the set of node values  $\mathbf{H}$ . The response ( $\mathbf{O}$ ) of the network can be formalized as the matrix product between  $\mathbf{H}$  and a vector of weights  $\boldsymbol{\beta}$ , namely  $\mathbf{O} = \mathbf{H}\boldsymbol{\beta}$ . Training is performed only on the output response by determining the vector  $\boldsymbol{\beta}$  that allows obtaining a given target ( $\mathbf{T}$ ). As a result, the smallest norm least squares solution is  $\boldsymbol{\beta} = \mathbf{H}^+\mathbf{T}$ , where  $\mathbf{H}^+$  is the Moore-Penrose generalized inverse of  $\mathbf{H}$ . It is proven that ELM has the universal approximation ability and can reproduce any output with enough nodes.

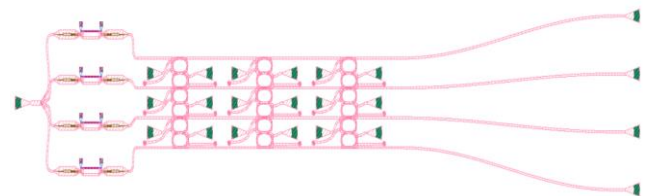


**Figure 40:** Top view of the optical design used to implement the ELM algorithm.

In this work we have studied the implementation of ELM in an integrated circuit. Figure 40 shows the top view of the network design. It consists of single mode channel silicon waveguides highlighted in figure with the red lines. The network can be divided into three parts: an input layer, a hidden layer consisting of an array of coupled microresonators, and a calibration layer. Light coupling and information encoding take place in the input layer. Encoding is achieved by splitting the input laser into four signals and applying intensity modulation using Mach-Zehnder interferometers controlled by microheaters. On the other hand, the calibration layer is only for network response monitoring. The hidden layer is the main part of the structure. It is here that the information processing takes place

and, thus, the generation of the response matrix  $\mathbf{H}$  occurs. This matrix is composed of the values obtained from the measurement of the intensity of the light scattered by the 18 gratings connected to the 18 microresonators. The measurement is done by recording the light scattering with an infrared camera placed above the optical chip. Training the network consists in determining the  $\beta$  weights that minimize the matrix expression  $\mathbf{H}\beta-\mathbf{T}$ . It is performed off-line through a PC by means of the ridge regression algorithm. Note that the network can represent the ELM algorithm by considering that: the weights of the  $\mathbf{H}$  matrix are given by the couplings between microresonator/microresonator and microresonator/waveguide. These weights are random, since by design all the couplings are equal, and consequently, they differ only for the stochastic fabrication errors.

The optical network was tested with both two-level and multi-level tasks for different wavelengths of the input laser. The two-level tasks consist of logical operations: AND, NAND, OR, and XOR. Here, the encoding of the information has been implemented by using only two of the four input ports of the network. The maximum of the signal amplitude was used as bit 1 and 30% of the maximum as bit 0. Specifically, we have tested all permutations of the input ports by sending each excitation combination, i.e., [00, 01, 10, 11], four times. Only one of the excitation combinations has been used to train, while the other three have been used to test, resulting in a ratio of 20/80. The network solves all logic operations. In particular, the XOR is solved both outside and inside the resonant wavelength range of the microresonators matrix. For this task, the 18 microresonators are therefore an excessive number of nodes. In fact, without taking advantage of ridge regression training, we have shown that the XOR can be solved with only one microresonator for a few input wavelengths.

The multilevel tasks we used to test our network are iris flower recognition and banknote recognition. Both tasks present a database characterized by four features. For the iris dataset, these are the length and width of the petal and sepal. The information is encoded by using one input port for each feature. The values corresponding to a given feature are scaled between the maximum and 30% of the maximum optical intensity. Each input flower or banknote was sent to the network seven times in random order. Monte Carlo cross-validation is used for training and testing. The dataset used is split 70% to train and 30% to test. This procedure was repeated 100 times, each time changing the elements belonging to the training set and those belonging to the test set. Here, the  $\mathbf{H}$  matrix is the average of the light scattered by the 18 microresonators. In the case of the iris flower, the network must distinguish between the three species of iris: Setosa, Versicolor and Virginica. On the other hand, for the banknote task, the network must have an answer as to whether the banknote is

true or false. By using three bases: one for each type of flower and, therefore, by using three ridges and by following as the decision approach the winner takes all scheme. The neural network improves the classification rate by more than 10%, showing a maximum value within the resonance region of  $(96.5 \pm 0.2) \%$ . In the case of banknotes, the best classification rate obtained by the network is  $(97.9 \pm 0.2) \%$ . Note that the theoretical limit in this case is about  $(97.6 \pm 0.2) \%$ .

### 13. Effect of the global thermal cross-talk on a photonic feed-forward neural network (Stefano Biasi, Riccardo Franchi and Davide Bazzanella)

In integrated optics, microheaters are used to induce a localized temperature change, thereby varying the refractive index via thermo-optic effect. When placed on top of a waveguide, they form a phase shifter. This is an optical component that changes the phase of the optical field, allowing any linear spatial optical transformation to be implemented. Despite the energy efficiency of silicon phase shifters, they generate heat flow through the substrate. As a result, a microheater affects the overall temperature of the integrated circuit, not just the local temperature of the device to which it is connected. This can affect the response of optical components and delay the reaching of steady states, especially for microresonators or unbalanced Mach-Zehnder interferometers.

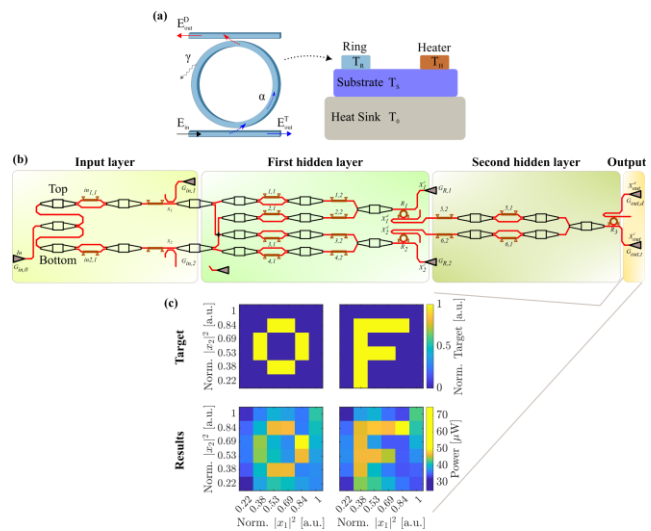


**Figure 41:** (a) Sketch of a microresonator and the four blocks that are used to model the heat exchange between the microheater and the microresonator. (b) Feed-forward neural network top view. The network consists of four layers: input, hidden and output. Three microresonators provide the nonlinear activation function. (c) Target (top) and experimental (bottom) map for an "O" shape and an "F" shape.

In this work, we show how microheaters can affect the response of microresonators even when placed at a distance

of about one millimeter. We link the local and global effects of induced thermal variation to the nonlinear response of a microresonator/bus waveguide system. Using the model of Figure 41 (a), consisting of four blocks: a microresonator, a substrate and a heat sink, we have studied the interaction between a microheater and a microresonator more than 200  $\mu\text{m}$  away. Substrate means the material between the microresonator and the heat sink: it can be the bare wafer substrate or the package when the chip is placed in a ceramic handler. The model is based on the heat exchange between the four blocks. It is formalized by Newton's law of cooling. On the basis of the modeling and the experimental characterization, we have found that a microresonator placed in a ceramic package and affected by the temperature of a microheater has a thermal relaxation time constant of about 220 ms. Thus, the microresonator reaches a steady state in about 1 s. These values are characteristic of the system and do not depend on the actual distance between the optical components when considering distances larger than 200  $\mu\text{m}$ . We have shown experimentally that such global thermal effects are so effective that even a distant microheater can drive a microresonator into self-pulsing oscillations. In addition, we experimentally demonstrate the limitations of using phase shifters in an all-on-chip feed-forward neural network (FFNN) that uses microresonators as the activation function.

The FFNN, shown in Figure 41 (b), encodes information and processes the signal within the silicon circuit via phase-shifters implemented by microheaters. The training is done by supervised learning through minimization of a cost function by a free gradient algorithm. The FFNN allows the emulation of a nonlinear function defined from the  $\mathbb{R}^2$  domain set to the  $\mathbb{R}$  codomain one. Consequently, as shown in Figure 41 (c), it reproduces nonlinear shapes, such as an "O" or an "F", identified by a threshold between target elements with value 0 and 1. Figure 41 (c) shows, at the top, the target map of an "O" and an "F" shape, while those at the bottom report the experimental response of the network after the training procedure. The FFNN seems to solve both tasks, learning an "O" and an "F" shape, since the experimental measurements show a clear difference between elements with target value 1 and 0. However, we have shown that the neural network, in a supervised learning process, uses the global heat generated by the microheaters in the input layer to solve the task. It is noteworthy that the distance between the microheaters in the input layer and the microresonators is more than 800  $\mu\text{m}$ . Despite this distance, the encoding of information by a specific pattern combined with the used time scale induces the network to use the microresonators as filters. This was explained by implementing the influence of "local" and "global" temperature variation in the nonlinear response of a microresonator. Here, the term "local" refers to the temperature of individual optical components,

such as the microheater and the microresonator. In contrast, the term "global" refers to the temperature of large regions of the entire optical circuit, which includes the substrate temperature and is affected by the variations of the local ones.

#### 14. Interferometric cavity ringdown for ultrahigh Q-factor microresonator (Stefano Biasi and Riccardo Franchi)

Microresonators are one of the key building blocks of integrated photonics. Their strength lies in their ability to store high field intensity, which enhances light-matter interactions. This allows them to improve both classical and quantum phenomena. Examples include slow light transmission, narrow linewidth light generation, frequency combing and entanglement generation. The fingerprint of an microresonator is the quality factor (Q). It quantifies the ability of the microresonator to store energy. In recent decades, advances in fabrication processes have led to the realization of increasingly high performance microresonators. Recently, a record value of 422 million intrinsic Q was demonstrated using a silicon nitride ring microresonator. These ultra-high quality microresonators have as a limiting factor the surface wall roughness, which induces arbitrary backscattering of light. As a result, the transmission spectrum does not exhibit the usual Lorentzian shape, but a resonance doublet induced by the interaction between the counter-propagating modes. Consequently, standard methods for estimating the quality factor are not applicable due to the energy exchange between the clockwise and counterclockwise modes.

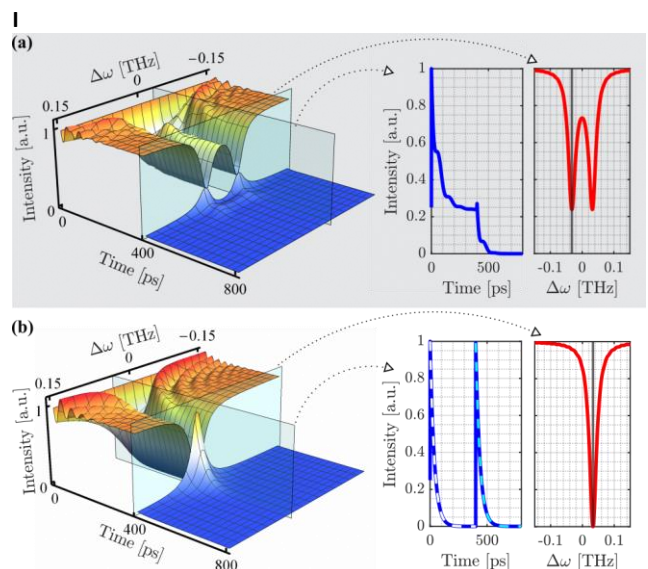


**Figure 42:** Response of the microresonator/bus waveguide system for Hermitian coupling between the counterpropagating modes as a function of time and frequency detuning. Specifically, (a) and (b) show the outgoing field intensity for single-side and interferometric excitation, respectively. Under the right conditions, a doublet merges into a single Lorentzian, allowing the quality factor to be estimated

In this work, we show theoretically that in the presence of

a resonance doublet, the interaction between the clockwise and counterclockwise modes distorts the exponential decay of the temporal response by introducing an intensity oscillation. This makes the application of common cavity ring-down techniques inaccurate. In addition, we show theoretically how an interferometric excitation can overcome this problem. In fact, under the right conditions, it allows to merge a resonance doublet into a single Lorentzian. A classic cavity ring-down method can then be applied. Thus, by simultaneously exciting the counter-propagating modes, the time response can be reduced to the usual dynamics of a single-mode microresonator unaffected by backscattering. Consequently, the Q of a microresonator can be defined by estimating the photon lifetime and, therefore, only by measuring the charging and discharging times. This is shown in Figure 42 for the Hermitian coupling between the counterpropagating modes. In particular, Figure 42 (a) shows the intensity of the outgoing field as a function of time and frequency detuning of the input laser. For single-side excitation, the spectral response is a balanced doublet (see spectral cross-section on the right). Note that the charging and discharging times are characterized by fast oscillations with an exponential trend. By performing an interferometric excitation, one can merge the doublet as shown in the outgoing field intensity of Figure 42 (b). This response allows to estimate the ultimate quality factor from the clear exponential dip (see the time cross-section on the right). By "ultimate" we mean the Q in the absence of the backscattering phenomenon. This result is demonstrated even for a general non-Hermitian coupling.

### 15. The infinity loop microresonator: a novel integrated photonics structure to work at an exceptional point (Riccardo Franchi, Stefano Biasi and Diego Piciocchi)

The simplest physical systems can be modeled by a Hermitian Hamiltonian. In these systems energy is conserved and the eigenvalues of the system are real. If one wants to describe more complex systems, e.g. characterized, by losses and asymmetric couplings, a non-Hermitian matrix must be used. Non-Hermitian systems are non isolated and generally have complex eigenvalues.

A Hermitian degeneracy is called diabolic point (DP) and is characterized by equal eigenvalues and always orthogonal eigenvectors. A particular degeneration, called exceptional point (EP), occurs in a non-Hermitian system and is characterized by the coalescence of both the eigenvalues and eigenvectors of the system.

In the literature, it is reported that particular features can be obtained in exceptional point structures, such as enhanced sensors, unidirectional lasers, unidirectional reflectors, and nonreciprocal optical components that exhibit a violation of the Lorentz reciprocity theorem.

Due to the presence of these perspectives, we have realized in an integrated silicon chip a new structure called Infinity-Loop Microresonator (ILMR) that works at an EP. The ILMR consists of an infinity-shaped waveguide coupled in both its lobes to the bus waveguide, see Figure 43.

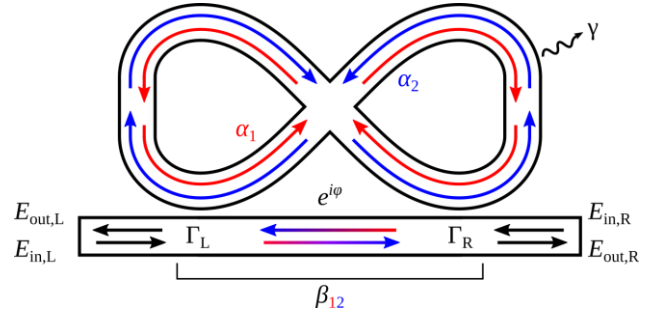


**Figure 43:** Sketch of the Infinity-Loop Microresonator (ILMR). All the coefficients are described in the text.

The coefficients  $\Gamma_L$  and  $\Gamma_R$  are the coupling rates between the bus waveguide and the left/right lobe of the infinity-shaped waveguide.  $\gamma$  is the intrinsic loss rate of the ILMR and  $\varphi$  is the phase acquired by the wave which propagates in the bus waveguide between the two lobes of the infinity-shaped microresonator.

Figure 43 shows that the ILMR can be modeled as a system characterized by two counter-propagating modes ( $\alpha_1$  and  $\alpha_2$ ).  $\alpha_1$  is always the first excited by the bus waveguide and can transfer energy to the second mode ( $\alpha_2$ ,  $\beta_{12} \neq 0$ ) passing through the waveguide between the two lobes. Instead,  $\alpha_2$ , near the coupling region, is directed towards the border of the ILMR, and therefore, the wave coupled to the bus waveguide goes to the exit of the system (one of the two sides of the bus waveguide). As a result,  $\alpha_2$  does not transfer energy to  $\alpha_1$  ( $\beta_{21} = 0$ ). Thus, if we write down the Temporal Coupled Mode Theory equations, we obtain:

$$i \frac{d}{dt} \begin{pmatrix} \alpha_2 \\ \alpha_1 \end{pmatrix} = H \begin{pmatrix} \alpha_2 \\ \alpha_1 \end{pmatrix} - \begin{pmatrix} \sqrt{2\Gamma_R} e^{i\varphi} & \sqrt{2\Gamma_L} e^{i\varphi} \\ \sqrt{2\Gamma_L} & \sqrt{2\Gamma_R} \end{pmatrix} \begin{pmatrix} E_{in,L} \\ E_{in,R} \end{pmatrix},$$

where the system Hamiltonian is:

$$H = \begin{pmatrix} \omega_0 - i\gamma_{tot} & -i\beta_{12} \\ 0 & \omega_0 - i\gamma_{tot} \end{pmatrix}.$$

$\gamma_{tot} = \gamma + \Gamma_L + \Gamma_R$  is the total loss rate and  $\beta_{12} = 4e^{i\varphi} \sqrt{\Gamma_L \Gamma_R}$ .

It is evident that  $H$  is non-Hermitian; in fact, there is an asymmetric coupling ( $\beta_{12} \neq 0$ ,  $\beta_{21} = 0$ ). Moreover, by deriving the eigenvalues and eigenvectors of the system we obtain that both coalesce:

$$\lambda_1 = \lambda_2 = \omega_0 - i\gamma_{tot}$$

$$v_1 = v_2 = \begin{pmatrix} 1 \\ 0 \end{pmatrix} \Rightarrow \langle v_1 | v_2 \rangle = 1.$$

Thus, since the ILMR is a non-Hermitian system characterized by the coalescence of the eigenvalues and of the eigenvectors, it works at an EP. As a result, the ILMR is completely different from a usual/standard microring resonator (MR). The MR is also characterized by coincident eigenvalues but at the same time its eigenvectors are orthogonal and consequently, the MR works at a DP.

We then compared the ILMR with the MR. The ILMR unlike the MR can have different spectral responses in reflection depending on the side from which the system is excited. By introducing a small Hermitian perturbation ( $\delta\beta$ ), which may be for example due to the presence of a molecule we want to detect, the eigenvalues of the two structures change. In the case of the MR, there is a linear dependence as a function of  $\delta\beta$ ,  $\lambda_{1/2} = \omega_0 \pm |\delta\beta| - i\gamma_{\text{tot}}$ . In contrast, the splitting of eigenvalues for the ILMR, for small perturbations, has a square-root dependence as a function of  $\delta\beta$ ,  $\lambda_{1/2} = \omega_0 \pm \sqrt{(\beta_{12} + \delta\beta)\delta\beta^*} - i\gamma_{\text{tot}}$ . As a result, the square-root trend, characteristic of EPs, has a higher sensitivity than the linear trend, characteristic of DPs.

In conclusion, we introduced a new integrated microresonator (the ILMR) that works on an EP. We will then be able to exploit the special features of EPs, such as enhanced sensitivity, to build innovative devices.

#### 16. Towards topologically protected states (Bülent Aslan, Salamat Ali, Riccardo Franchi, Alberto Munoz De Las Heras and Stefano Biasi)

In the realization processes of integrated photonics, on-chip topological photonic devices offer great promise for applications. The field is opening up new opportunities for new device functionalities with both theoretical and practical challenges. The intention of this study is to investigate the non-Hermitian topological photonics.

For this purpose, we have designed on-chip arrays of microresonators consisting of both taiji and conventional microresonators. Figure 44 (a) shows the basic plaquette consisting of two taiji microresonators coupled to a single microresonator. The red lines are single-mode silicon waveguides, while the triangles represent gratings for coupling incoming and outgoing light. This simple structure can be easily extended to more complex structures as shown in Figure 44 (b-c). Here, by playing with the phase difference between the counter-propagating modes, it is possible to build artificial Hamiltonians. This allows to introduce both counterintuitive behavior in transmission and/or reflection, and to generate topologically protected modes in such complex designs (as in Figure 44 (c)). The use of taiji makes it possible to exploit the properties of the exceptional points in the energy exchange between clockwise and counterclockwise modes. The performance of the exceptional points is compared with that of the diabolic points, typical of conventional microresonators, by the plaquette in Figure 44 (d). They have a cut S-shaped

waveguide ending in an inverse taper. In this way, Taiji and conventional microresonator present the same losses. The creation of all these structures requires a robust formulation of a general framework that is expandable for more complex structures by using the coupled mode theory formalism.

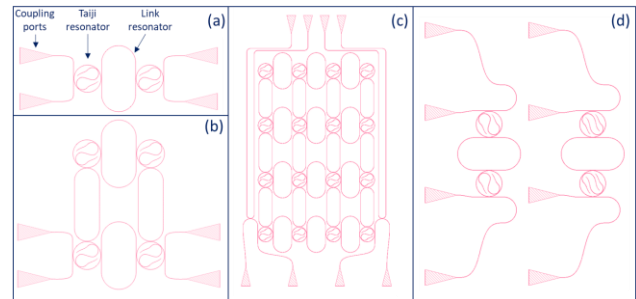


**Figure 44:** Representative plaquettes on the chip designed for topological photonic studies. The building blocks of the plaquettes are the Taiji micro-resonators connected with link-resonators in different array sizes; (a) 2x1, (b) 2x2 and (c) 4x4. The chip also has control structures where the inner S-shaped waveguide is broken (d).

#### 17. Undetected photon interference measurements on a silicon chip (Chiara Micheli)

In classical gas spectroscopy, a gas sample is probed with light: detecting the light that has interacted with the gas, allows deriving various properties of it. Undetected photon measurement is a quantum measurement technique that permits to derive these properties without the need of any detector to operate at the wavelength of the probing light. This enables the possibility of choosing the probe wavelength within a range for which suitable detectors are not available. A spectral region of great interest for spectroscopy is the mid-infrared (MIR): many gas molecules have their fundamental absorption bands in the MIR (2  $\mu\text{m}$  - 20  $\mu\text{m}$ ), however, optical instruments working in this spectral region are both bulky and expensive. Detectors, for example, have a main limitation since they are sensitive to the thermal noise due to black body radiation of the detector itself and must be kept at low temperatures, resulting in expensive and bulky devices. For these reasons, an efficient MIR detection is a concrete need that finds its application in gas sensing and environmental monitoring.

A spectroscopy measurement can be done by placing the gas sample between two identical photon sources. If a MIR photon is generated in the source coupled to the gas chamber, it will interact with the gas. For example, it will be transmitted with a certain probability amplitude  $t$  and it will acquire a phase  $\gamma$ . On the contrary, when the photon is generated in the other source, it does not interact with the gas. If the two photons are indistinguishable, there is no way to know which one of the two sources emitted it, so there is no way to know if a photon had interacted with the

gas sample or not. This lack of information leads to an intensity interference, characterized by a visibility  $t$ , that maps the phase difference  $\gamma$ : the interference pattern reveals the presence of the gas and give information about its refractive index and absorption coefficient.

In the undetected photon technique, the photon sources are two nonlinear optical sources, each of which emits a pair of entangled photons. The quantum entanglement between the generated photons plays a key role in the measurements: the photon that interacts with the gas remains undetected, but the signature of its interaction can be revealed by detecting the entangled photon partner, that have never interacted with the sample. The nonlinear sources can be engineered in order to generate the photon that interacts with the gas in the MIR and its entangled photon in a spectral region where the detection is efficient. Our experiment deals with undetected photon interference measurements on a silicon chip. Via intermodal spontaneous four-wave mixing in multimode silicon-on-insulator waveguides, we generated pairs of near-infrared/mid-infrared entangled idler/signal photons, as schematized in Figure 45.

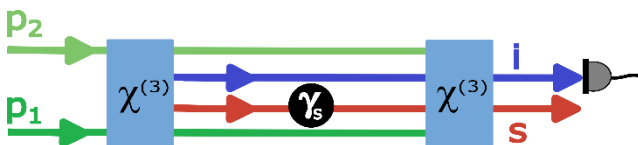


**Figure 45:** Scheme of the experiment. Two  $\chi^{(3)}$  nonlinear sources are coherently pumped with two classical beams ( $p_1$  and  $p_2$ ) and two pairs of photons, idler ( $i$ ) and signal ( $s$ ) are generated via intermodal spontaneous four-wave mixing. The pump beams are in the transverse electric (TE) polarization, in the fundamental (TE0) and in the first excited (TE1) optical mode, at wavelength 1570 nm. The idler photons are generated in the TE0 optical mode at wavelength 1290 nm, while the signal photons are in the TE1 optical mode, at wavelength 2  $\mu\text{m}$ . The paths of the generated photons are superposed and the sources are identical, such that the photon pair generated in one source is indistinguishable with respect to the pair generated in the other. Between the two sources, we vary the phase of the signal photons.

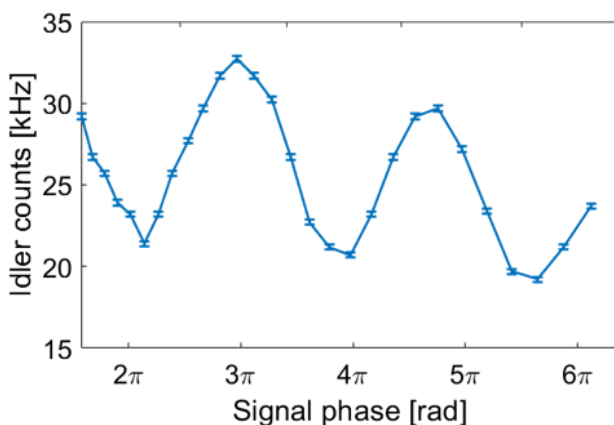


**Figure 46:** Interference pattern observed in the idler counts, varying the phase of the signal photons between the two sources.

Varying the phase of the signal photons generated in one source, we observed an interference pattern detecting the entangled idler photons, as shown in Figure 46.

### 18. High-performance CMOS-compatible integrated photonic devices for quantum circuits at near-visible wavelengths (Matteo Sanna, Alessio Baldazzi and Stefano Azzini)

A large number of integrated photonic components and systems have been fabricated and commercialized at telecommunication wavelengths, enabling the application of these devices in numerous areas. The most recent one is that of quantum computing, and specifically the realization of integrated quantum simulators. These are parametrized quantum circuits that can be used to simulate even complicated quantum systems, relevant to solid-state physics, biology, and chemistry, making it also possible to solve problems that are challenging or practically impossible for classical computers. In this context, integrated photonics has the potential to eliminate the need of cryogenic systems, typically necessary for other quantum platforms, by choosing photonic materials that can operate at room temperature, thus making such quantum devices more accessible. Along this direction, as part of the European project EPIQUS (Electronic-Photonic Integrated Quantum Simulator Platform), we are working on the development of an integrated photonic platform enabling monolithic co-integration with silicon photodiodes, CMOS-based electronic circuits and in particular with single-photon avalanche diode (SPAD) detectors made of silicon and thus operating in the VIS-NIR region at room-temperature. To this aim, we have been working on two materials transparent at near-visible wavelengths, Silicon Oxynitride (SiON) and Silicon Nitride (SiN), to be used for both the generation and manipulation of quantum light. For the development of affordable and performant integrated photonic devices that operate even at visible wavelengths, SiN and SiON represent extremely promising platforms.

Here we present some results of linear characterization of integrated SiN and SiON photonic devices designed to work around 750 nm and fabricated by a low-pressure chemical vapour deposition (LPCVD) technique. These devices can be used for the fabrication of various components such as integrated filters, Mach-Zehnder interferometers (MZIs) and multimode interference (MMI)-based couplers, which are of particular interest for the realization of high-performance quantum circuits.

The devices were designed and, after fabrication, characterized between 700 and 800 nm using a supercontinuum laser. The coupling losses are 8 dB/facet for SiN and 11 dB/facet for SiON. The propagation losses are about 1.8 dB/cm and 1.7 dB/cm, for SiN and SiON respectively. Different structures were designated and characterized: MMIs, asymmetric MZIs (aMZIs), crossings and curves of

different radii. In this contribution, we will focus only on the first two structures. The first structure is a 2X2 MMI (Figure 47(a)). The results of the characterization of insertion loss (red curves) and splitting ratio unbalance (black curves) are shown in Figure 47(b) and 47(c), for SiN and SiON respectively. For SiN, an MMI (Figure 47(b) with a rather flat

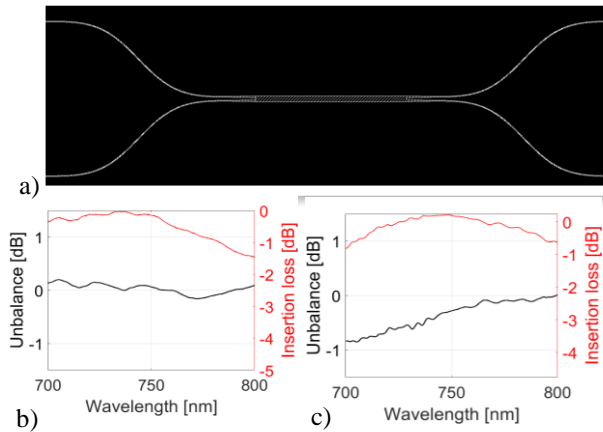


**Figure 47:** a) Layout of a 2x2 MMI-based beam splitter. (b)-(c) Characterization of MMI splitters: (b) SiN, (c) SiON. The black curve shows the unbalance between the two output ports (out2/out1). The red curve shows the insertion loss.

unbalance within 0.25 dB is observed, and a minimum record value of 0.05 dB at 740 nm. The insertion loss is minimal around 740 nm, as designed, with a record value of 0.05 dB. For SiON, an MMI (Figure 47(c)) is reported with an unbalance within 0.8 dB in the 700–800 nm region, and a minimum value of 0.4 dB at 740 nm. Insertion loss shows a minimum value of 0.03 dB. The asymmetric Mach-Zehnder interferometers (aMZIs) are the second structure we want to focus on. These devices consist of two MMIs connected by waveguides of different length, and in one of the two arms of the MZI a heater can be found, used to control an additional phase between the two arms (Figure 48(a)) via thermo-optic effect. aMZIs are very useful for wavelength filtering purposes. Figure 48(b) reports the transmission spectrum of a SiN integrated filter designed for rejecting the pump wavelength of a spontaneous four-wave mixing (sFWM) process: it is made of four cascaded aMZIs using MMI-based beam splitters. This passive (i.e. with no heater) aMZI-based filter has an apparently good tuning between the four aMZIs, featuring a regular free spectral range (FSR), an insertion loss of less than 3 dB and an effective rejection ratio of roughly 22 dB. As another example, Figure 48(c) displays the normalized transmission spectra of the output ports of a single aMZI that will be used to spectrally separate quantum-correlated signal and idler photons from sFWM in SiON waveguides. This filter features an insertion loss close to 0 dB, and its FSR is in good agreement with respect to what designed via FDTD simulations.

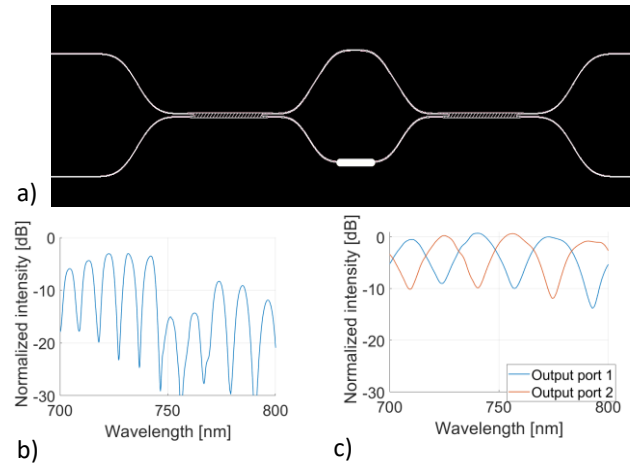


**Figure 48:** a) Layout of a single aMZI. b) Transmission spectrum of four cascaded aMZIs in SiN waveguides. c) Transmission spectrum of an aMZI in SiON waveguides.

These devices represent a few examples of the main high-performance building blocks needed to build integrated quantum photonic circuits that can manipulate and filter quantum states of light.

We acknowledge collaborators of the I&QO group at FBK for the fabrication of the photonic devices within the European project EPIQUS.

### 19. Design of a variational quantum eigensolver on a silicon photonics chip (Alessio Baldazzi, Matteo Sanna and Stefano Azzini)

Many applications (material science, drug discovery, complex molecular dynamics) require the calculation of the ground state energy of a molecule. Because of the limitations of the Noisy Intermediate Scale Quantum era, completely quantum algorithms requiring deep circuits, like Quantum Phase Estimation (QPE), are still prohibitive. However, in 2014, Peruzzo et al. proposed the Variational Quantum Eigensolver (VQE) using much shallower circuits where a CPU controls the quantum hardware and manages the raw data about expectation values of the qubits configurations.

The VQE algorithm starts with the encoding of Hamiltonian in the Pauli operator basis. After this procedure the Hamiltonian is written as a linear combination of Pauli matrices and their products:

$$\mathcal{H} = \sum_{i\alpha} h_{i\alpha} \sigma_{i\alpha}^x + \sum_{i\neq j} h_{ij}^{\beta\gamma} \sigma_{i\beta}^x \sigma_{j\gamma}^y + \dots$$

The task of the quantum hardware consists of preparing a generic state and producing the statistic to construct the expectation value of the Pauli operators present in the Hamiltonian. Then the CPU, which knows the coefficients  $h$  contained in the Hamiltonian, uses the expectation values

of the Pauli operators to calculate the expectation value of the full Hamiltonian. The latter quantity constitutes the cost function of the problem, which the CPU calculates at every run of the quantum hardware. Therefore, the CPU manages and updates the quantum hardware to prepare new trial states to achieve the minimization of the cost function. The algorithm ends when the target precision is achieved in the evaluation of the ground state energy, which by definition should be the global minimum of the cost function given by the Hamiltonian. The advantage of this approach consists in the fact that the coherence time for a single manipulation and measurement does not depend on the precision and thus we need a limited circuit depth without error correction. However, we pay this advantage in total computation time, since the total number of iterations grows quadratically with the inverse of the precision.

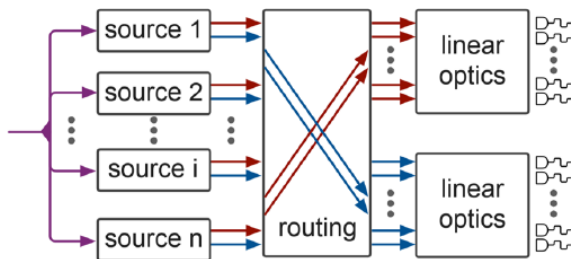


**Figure 49:** Schematic layout of the quantum hardware for the VQE. Programmable phase shifters, MMIs and crossing waveguides compose the routing and manipulation part, while the sources of photon pairs are based on spontaneous four-wave mixing in silicon photonics waveguides.

We have designed the quantum hardware for a silicon photonics implementation of the VQE algorithm, with the schematic structure shown in Figure 49. The circuit can be thought of as divided into different parts. Firstly, the pump is coherently split using Mach Zehnder interferometers (MZIs) made of multi-mode interference devices as beam splitters and metal heaters as thermo-optic phase shifters. The superposition of pump photons excites the identical sources made of spirals and a superposition of pairs of photons, called idler and signal, is created in the array of parallel waveguides through intra-modal spontaneous four-wave mixing process. The couple of nondegenerate photons is deterministically separated using an asymmetric MZI and spatially separated through a network of waveguides crossings. At the end of routing stage, we prepare two entangled qudits, whose Hilbert space has the same dimension of  $2C$  qubits where the number of sources  $n = 2^C$ . Then the entangled qudits are manipulated and projected on a specific exit using a triangular scheme of MZIs and the pump is filtered out before the detection. The triangular network has been chosen because it scales logarithmically with the number of sources and reduces to two the number of filters and detectors, independently from

the the number of sources. However, to retrieve all the correlations, the procedure for one trial state must be repeated  $n^2$  times.

Our design of a silicon photonics chip will work with four sources, which means two ququarts or equivalently four qubits. The first benchmarking will consist of finding the ground state energy and the electronic configuration of the Hydrogen molecule. This case is characterized by the fact that the cost function depends on only one parameter, which controls the amount of contribution of the anti-bonding orbital to the equilibrium configuration. Once this benchmark is achieved, the circuit will be used also to solve small classical combinatorial problems.

## 20. Straight waveguides or ring resonators? An analytic comparison to find out the best source at interfering quantum light (Alessio Baldazzi, Matteo Sanna and Stefano Azzini)

On photonic platforms, the number of qubits is typically associated with the number of single photons, whose quality is quantified intrinsically by their purity and extrinsically by their indistinguishability. The demand for 'good' physical qubits translates into the engineering of 'good' sources of photons. What type of source performs better among the probabilistic sources is a crucial question. In addition, the limited amount of physical qubits in the Noisy Intermediate Scale Quantum (NISQ) computing era prevents the development of error-correction techniques as well as universal quantum computing hardware, and brings people to work with quantum simulators, i.e. devices that perform non-universal and problem-focused algorithms. Therefore, an interesting question about different types of probabilistic sources would be: which is the most suitable source of photons given the requirements of the specific algorithm? Indeed, a final close-term aim could be the realization of a source library, which can be consulted as needed, and updated with the improvements of the sources present in the list. In this way, in the NISQ computing on a photonic platform, one can eventually choose the kind of source depending on which class of problems is targeted and how many resources are available.

Regarding the evaluation of the indistinguishability, we decide to consider the scheme represented in Figure 50. The circuit is composed by a Mach-Zehnder interferometer (MZI) which contains two different sources in parallel. In particular, we find ring resonators and spiral waveguides, that can produce couples of frequency-degenerate photons through the intra-modal four-wave mixing process excited by two pump lasers with different wavelengths. We can imagine using the heaters present on the ring resonators to tune their resonances on and off with respect to the pump lasers wavelengths and obtain the resonant and non-resonant dynamics on the same structure.

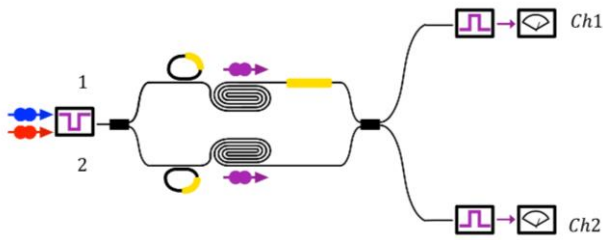


**Figure 50:** Schematic layout. The sources in the two arms of the MZI are composed of spirals or rings.

The MZI contains also a tuneable phase shifter: in this way, the sources are coherently excited and their relative phase can be controlled before the last MMI. Finally, the generated photons are selected by the pass-band filters before the detection.

Since we work in a low squeezing regime, the state present after the two sources is a superposition of pairs of photons generated by the two sources. Such situation is the initial state for Reverse Hong-Ou-Mandel (HOM) experiment, where the superposition of pairs of identical photons anti-bunches on a MMI. In our case we can tune the interference by changing the phase of the phase shifter present after the upper source of Figure 50. The more identical the sources are, the more intense the interference pattern will be when the relative phase term entering in the quantum state is varied. Therefore, the key figure of merit is given by the normalized coincidence rate as a function of that relative phase.

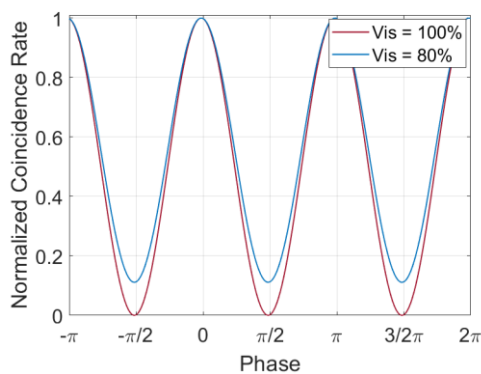


**Figure 51:** Coincidence of photon pairs of the MZI with two different the two type of sources depending on the phase  $\phi$  of the MZI.

We have constructed a theoretical model to link the visibility given by the coincidence rate to the overlap of the Joint Spectral Amplitudes (JSA) relative to the two sources. Since the sources are not independent, in the low squeezing regime the visibility does not depend on the purity of single sources. This means that even if purity is lower and the generation band is broader, what matters is how much the two JSA are similar. In Figure 51 we show two different cases of visibility: one with 100% of visibility or equivalently 100% of JSA overlap and another with 80% of visibility or

66% of JSA overlap. Such results tell us how much indistinguishable the pairs of photons are between the sources contained in the MZI of Figure 50. It is reasonable to think that a larger visibility can be achieved by non-resonant structures like waveguide spirals with respect to resonant devices like ring resonators. As a matter of fact, the latter features a few degrees of freedom that can affect the level of indistinguishability of distinct devices, e.g. due to the fabrication process. On the other hand, spirals are more robust against such issues, but typically their generation rate is lower with respect to the ring resonator case and the purity is constrained by how much narrow is the band-pass filter in use in the setup. As anticipated at the beginning, ideally one can choose the type of source depending on which characteristic is needed for the algorithm to be implemented. This brings to the idea of application-tailored sources, i.e. sources designed for a specific algorithm and chosen to balance the required properties and the implementation efforts.

Experiments on this topic are performed at ETRI research institute in South Korea, where we have a collaboration with Dr Jong-Moo Lee. In the future, we will generalize the scheme of Figure 50 in order to study the indistinguishability of a generic even number of photon pairs sources.

### 21. A SWAP-test algorithm for photonic quantum machine learning (Nicolò Leone, Alessio Baldazzi and Stefano Azzini)

In machine learning, one of the key concepts is represented by Kernel methods. They take their name from the Kernel function which stays at the core of supervised learning models associated with algorithms of regression and classification. Since a Kernel function can be written as a scalar product in the feature space, one among the different ideas of quantum machine learning consists in using a quantum hardware to evaluate Euclidean distances between the quantum representations of our data set. The advantage of this approach is due to the fact that there is an interesting analogy between the languages of machine learning (Kernel methods in particular) and quantum mechanics.

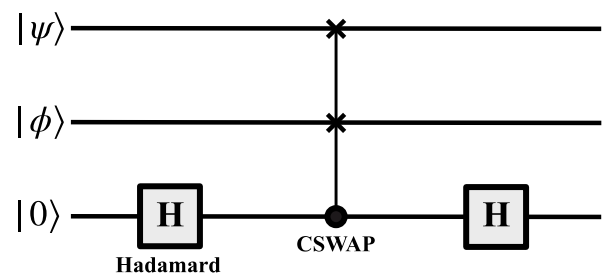


**Figure 52:** Schematic representation of a quantum SWAP-test circuit.

The algorithm we have chosen for a photonic implementa-

tion is the SWAP-test. Once a given set of data is represented as qubits, the purpose of the SWAP-test consists in finding the scalar product of two arbitrary states, and the resulting distance can then be fed as an input of a Kernel function. In principle, this quantum algorithm has a computational complexity of lower order with respect to classical algorithms: the number of samples needed to obtain an error  $\varepsilon$  with probability  $1-\delta$  scales as  $\frac{\log(1/\delta)}{\varepsilon^2}$ . The circuitual scheme of the SWAP-test algorithm is well known and it is reported here in Figure 52.

The starting point consists in initializing two quantum states  $|\psi\rangle$  and  $|\phi\rangle$ , with an additional auxiliary qubit set in the  $|0\rangle$  state. Then an Hadamard gate (H) is applied to the  $|0\rangle$  state to create a superposition of the states  $|0\rangle$  and  $|1\rangle$ . After this operation, a controlled swap (CSWAP) is applied to the state, with the aim of swapping the two other states when the auxiliary qubit is  $|1\rangle$ . In our silicon photonics chip, this CSWAP operation will be implemented using only linear optical integrated components, thanks to the exploitation of path-entangled single photon states. Lastly, it is necessary to apply another Hadamard gate operation to the auxiliary qubit. At the end of the circuit, it can be demonstrated that the probability of observing the state  $|1\rangle$  for the auxiliary qubit can be seen as the scalar product of the two states  $|\psi\rangle$  and  $|\phi\rangle$ . In a nutshell, our photonic implementation translates the problem of evaluating the scalar product into a boson sampling problem. This simple 2-qubit SWAP-test has the potential of being incredibly powerful: scalar products between two arbitrary wave-functions can be computed just by measuring the probability of observing a certain outcome, and computing capabilities can be increased e.g. by putting onto the same photonic chip a few 2-qubit or even 4-qubit SWAP test circuits, thus increasing the number of qubits available for data-encoding.

## 22. A Silicon Oxynitride photonic chip for the generation of quantum-certified random numbers (Nicolò Leone and Stefano Azzini)

Random numbers are fundamental tools at the hearth of any cryptographic protocol. Indeed, the entire security of encryption methods is based on the unpredictability of the sequence of numbers used to secret a private message. Moreover, random numbers have important practical applications also in simulation and gambling. Quantum random number generators (QRNGs) [1] are quantum devices used to generate real random numbers. Indeed, only the probabilistic description of quantum mechanics offers the natural framework in which randomness can be really obtained, with the potential of making QRNGs the first quantum devices to be mass-adopted. However, a barrier to their widespread diffusion in market products is simply their price: compared to classical RNGs, like algorithm-based RNG and noise-based RNG [1], QRNGs are still more

expensive, without offering considerable advantages in terms of speed. Furthermore, many QRNGs require a perfect characterization of the hardware used to effectively generate a good amount of randomness, not solving problems connected to the introduction of possible correlations in the generated sequence due to the aging of components or even to the malicious attack of an adversary.

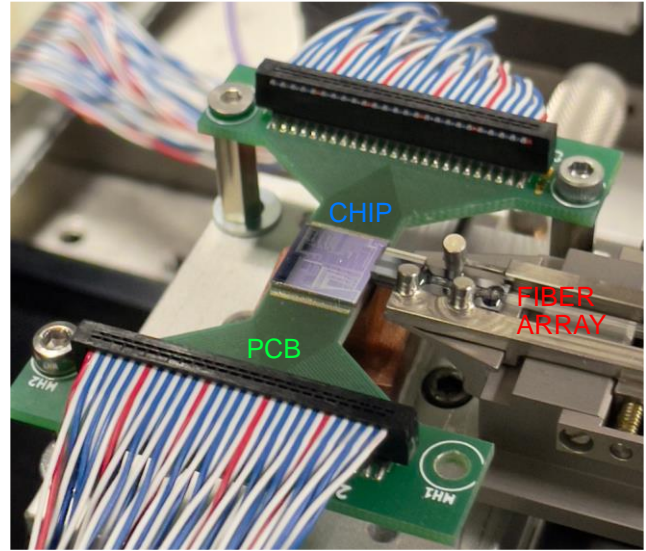


**Figure 53:** Picture of the experimental setup used to demonstrate our SDI-QRNG. Here are visible the integrated optical chip, the fiber array for light-coupling and the PCB used for electronically control the chip.

In the last few years, a new category of more secure QRNGs has been studied, semi-device independent QRNGs (SDI-QRNGs) [1], representing a reasonable compromise between feasibility of implementation and security. They can certify the produced randomness by exploiting fundamental laws of quantum mechanics, which act as randomness witnesses, at the cost of introducing only a partial characterization of the devices, limiting problems connected to unexpected behaviour of the hardware. Inspired by these developments, we have developed a Silicon Oxynitride photonic chip that can generate and manipulate path-entangled single-photon states starting from photons coming from an attenuated light source, even an incoherent one. The photonic device, the fiber array used for the in-out coupling and the control electronics are visible in Figure 53. On-chip the two qubits are obtained using path encoding: taking into account four waveguides, we use the relative and absolute positions of each waveguide with respect to the symmetry axis of the integrated circuit, as sketched in Figure 54(a) (with the symmetry axis represented by a white line). In particular, the absolute-position basis states are labelled as  $|U\rangle$ , and  $|D\rangle$ , where U stand for Up and D for Down. While  $|F\rangle$  and  $|N\rangle$  stand for Far and Near and determine the basis states of the second qubit. In this way, the first waveguide from the top of the chip is labelled as

$|UF\rangle$ , the second as  $|UN\rangle$ , the third  $|DN\rangle$  and the fourth as  $|DF\rangle$ . A single-photon entangled state of path  $(\frac{1}{\sqrt{2}}(|UF\rangle + |DN\rangle))$  is then generated by injecting light in the appropriate waveguides, using as an integrated 50:50 beam splitter a properly designed Multimode Interferometer (MMI) device (see Figure 54(b)). The relative phase  $\xi$  between the two states can be controlled by using two different thermo-optic phase shifters (PSs).

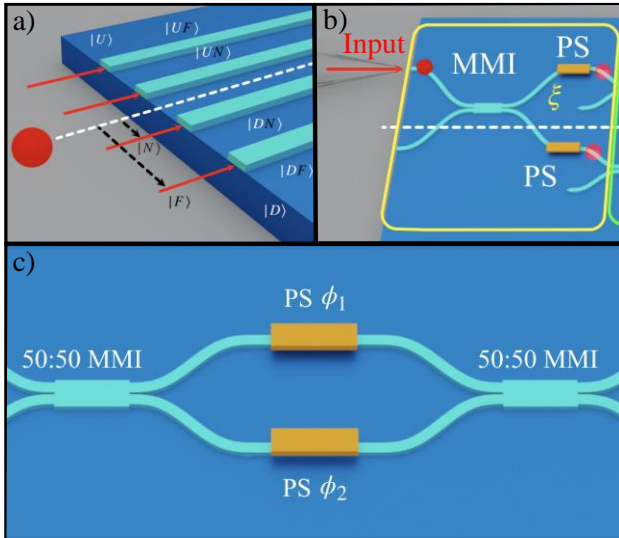


**Figure 54:** a) Two-qubit encoding using photon paths. b) Schematics part of the circuit necessary to generate path entangled states. c) Example of one integrated MZI used to control the relative and absolute position qubits

Random numbers are produced by performing Bell measurements on the generated SPE states by using a combination of various integrated Mach Zehnder Interferometers (MZIs). An example of the latter device is reported in Figure 54(c) and it is composed by two 50:50 MMIs and two PSs. Bell inequality violation is used as a randomness witness in the same manner as reported in [2]. Every time the outcomes of the different measurements induce a violation of the Bell's inequality, it is possible to certify the intrinsic quantum randomness of the result sequence or, equivalently, it is possible to lower-bound the min entropy of such a sequence. Physically, the violation of the inequality is due to the quantum contextual correlations between the different optical paths. To certify the randomness, partial characterization of the optical chip and of the (commercial) single-photon avalanche diodes used to detect photons have to be introduced. Min-entropy values as large as 30% are demonstrated. The experiment was performed using a red LED as light source, centered at 730 nm. The use of such a cheap and commercial light source, together with the integrated approach, paves the way to low-cost and intrinsically secure QRNGs, which have the real potential of being easily exploited e.g. in so-called Internet-of-Things devices to ensure communications security.

We acknowledge collaborators of the I&QO group at FBK for the fabrication of the photonic chip within the European project EPIQUS.

**For more info:**

Nanoscience Laboratory  
Department of Physics  
University of Trento  
via Sommarive 14  
38123 Povo- Trento (Italy)  
<http://nanolab.physics.unitn.it/>

Laboratory assistant  
Dr. Camilla Kandamulla A.  
email [c.kandamulla@unitn.it](mailto:c.kandamulla@unitn.it)  
phone +39 0461 283172